FU JEN STUDIES

NATURAL SCIENCES

NO. 17 1983

CONTENTS

FU JEN UNIVERSITY

TAIPEI, TAIWAN, REPUBLIC OF CHINA

DESIGN AND CONSTRUCTION OF MULTILAYER INTERFERENCE THIN FILMS WITH THE COMBINATION OF CeO_2 AND CRYOLITE

WEN-JEN LIN, KUNG-TUNG WU and JEN-I CHEN

ABSTRACT

The properties of optical interference thin films are discussed. Epstein's method is used to design the filters, and the concepts of equivalent index and thickness of equivalent layer are adopted. We design and manufacture high-pass, low-pass and band-pass multilayer interference filters with the combination of equivalent layers (L/2)H(L/2) and (H/2)L(H/2) of CeO_2 and cryolite. By using computer analysis, the pass-band of filters is discussed.

1. INTRODUCTION

Coating in the form of a thin film is an established phenomenon of modern physics which is being exploited both in basic research (the properties of matter) and for industrial applications. Recent advancements in theory and technology allow the production of more complicated and more efficient thin film systems.

It is the purpose of this paper to study the properties of optical interference thin films with the design and manufacture of high-pass, low-pass and band-pass multilayer interference filters for transmitting light within a certain wavelength range using non-absorbing films. Ivan Epstein's method is used to design the filters, and the concepts of equivalent index and thickness of equivalent layer are adopted. Each single layer can take its thickness and index of refraction as parameters to form a 2×2 characteristic matrix whose elements can be used to express the transmittance and reflectance of the whole multilayer.

The choice of thin film materials is of great importance for the production of reliable thin film products. We choose a high refractive index material CeO_2 in combination with a low refractive index material of cryolite (Na_3AlF_6) to form the multilayer interference

filters. The combination shall be confined to coatings produced by the high vacuum thermal evaporation technique.

The development of a thin film system always starts with a computer analysis. And predictions of stop-band or pass-band widths and positions are only as reliable as the numerical calculations of the computer program.

2. THE BASIC THEORY

A layered optical medium or multilayer extends in space from $z = z_a$ to $z = z_b$ $(z_a < z_b)$. The optical media in the regions $z < z_a$ and $z > z_b$ can be another multilayer, a substrate, or a surrounding medium. Figure 1 shows the construction of a typical multilayer interference filter.

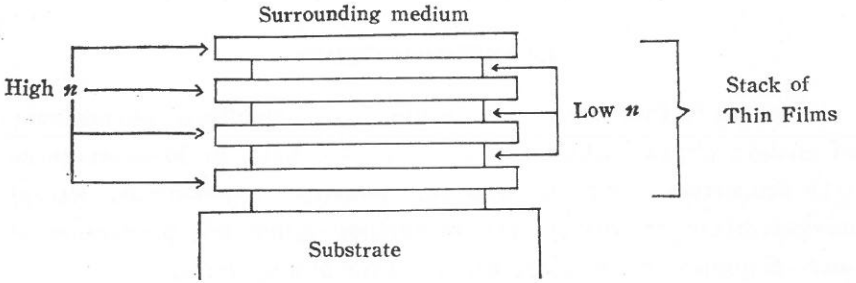

Fig. 1. Construction of a typical multilayer interference filter.

If a plane electromagnetic wave propagates in the z-direction, through this multilayer the electrical field $E(z_a)$ and the magnetic field $H(z_a)$ are related to the fields $E(z_b)$ and $H(z_b)$ by the following equation:

$$Q(z_a) = M(z_a - z_b)\, Q(z_b)$$

or

$$\begin{bmatrix} E(z_a) \\ H(z_a) \end{bmatrix} = \begin{bmatrix} M_{11} & iM_{12} \\ iM_{21} & M_{22} \end{bmatrix} \begin{bmatrix} E(z_b) \\ H(z_b) \end{bmatrix}, \quad \text{with } i^2 = -1. \qquad (1)$$

where the matrix elements are the solutions at the position $z = z_b$ of the following set of four simultaneous differential equations of the first order:

$$
\begin{aligned}
M'_{11} &= -(2\pi/\lambda)\, n^2(z)\, M_{12} \\
M'_{12} &= (2\pi/\lambda)\, M_{11} \\
M'_{21} &= (2\pi/\lambda)\, n^2(z)\, M_{22} \\
M'_{22} &= -(2\pi/\lambda)\, M_{21}
\end{aligned}
\qquad (2)
$$

with the initial conditions:

$$
M_{11}(z_a) = 1, \quad M_{12}(z_a) = 0, \quad M_{21}(z_a) = 0, \quad M_{22}(z_a) = 1. \qquad (3)
$$

We can conclude from Eqs. (2) that

$$
M'_{12} M_{21} + M_{11} M'_{22} = 0, \qquad M'_{11} M_{22} + M_{12} M'_{21} = 0,
$$

which means that

$$
\frac{d}{dz}(M_{11} M_{22} + M_{12} M_{21}) = 0,
$$

or

$$
M_{11} M_{22} + M_{12} M_{21} = \text{constant},
$$

and with Eqs. (3), then

$$
M_{11} M_{22} + M_{12} M_{21} = 1. \qquad (4)
$$

Eq. (4) is one of the properties of optical thin films.

The energy reflectance R and transmittance T for an optical coating can be calculated using the matrix theory developed by Abelès[1].

An optical thin film is characterized by its index n and mechanical (physical) thickness t. A flat, monochromatic wave of wavelength λ, passing through the film, normally undergoes a phase shift ϕ, where $\phi = 2\pi nt/\lambda$. The quantity nt is referred to as the optical thickness of the film. When phase shift ϕ is equal to $\pi/2$, the layer is said to be of the one-quarter wavelength type, and its optical thickness is one-quarter wavelength thick at $\lambda = \lambda_c$, where λ_c is referred to as the center wavelength of the layer.

A 2×2 matrix is associated with each layer, having the form

$$
m = \begin{bmatrix} m_{11} & im_{12} \\ im_{21} & m_{22} \end{bmatrix} = \begin{bmatrix} \cos\phi & (i/n)\sin\phi \\ in\sin\phi & \cos\phi \end{bmatrix}. \qquad (5)
$$

When the deposit comprises a stack of N layers, it is associated with a matrix equal to the product of the matrices associated with each layer. The matrix product is obtained according to the order of passage of the wave through the coating.

$$M = \begin{bmatrix} M_{11} & iM_{12} \\ iM_{21} & M_{22} \end{bmatrix} = \prod_{j=1}^{N} \begin{bmatrix} \cos\phi_j & (i/n_j)\sin\phi_j \\ in_j \sin\phi_j & \cos\phi_j \end{bmatrix}. \quad (6)$$

We assume that the coating is not absorbant. Coefficients M_{jk} are then all real and interlinked by Eq. (4). The complex reflection and transmission coefficients r and t_m of a plane electromagnetic wave propagating in the z-direction through the multilayer are given by[1,2]

$$\begin{aligned} r &= \frac{n_M M_{11} + in_M n_S M_{12} - iM_{21} - n_S M_{22}}{n_M M_{11} + in_M n_S M_{12} + iM_{21} + n_S M_{22}}, \\ t_m &= 2n_M(n_M M_{11} + in_M n_S M_{12} + iM_{21} + n_S M_{22})^{-1}, \end{aligned} \quad (7)$$

where n_S is the constant index of refraction for the substrate region ($z > z_b$), and n_M is the index for the surrounding medium ($z < z_a$).

From the above relations we can obtain the energy reflectance R and transmittance T as

$$\begin{aligned} T &= 1 - R \\ &= 4\left(2 + \frac{n_M}{n_S} M_{11}^2 + \frac{n_S}{n_M} M_{22}^2 + n_M n_S M_{12}^2 + \frac{1}{n_S n_M} M_{21}^2\right)^{-1}. \end{aligned} \quad (8)$$

According to Epstein[3], a multilayer system is broken down into a group of symmetrical multilayers, the equivalent index of refraction and thickness are established for each symmetrical multilayer, and their combinations are matched. The matrix of a symmetrical multilayer satisfies the condition $M_{11} = M_{22}$. We can define the following two quantities:

$$\begin{aligned} T_E &= \text{equivalent thickness} = \cos^{-1} M_{11} = \cos^{-1} M_{22}, \\ N_E &= \text{equivalent index} = +(M_{21}/M_{12})^{1/2}, \end{aligned} \quad (9)$$

which transforms Eq. (6) into

$$M = \begin{bmatrix} \cos T_E & (i/N_E) \sin T_E \\ iN_E \sin T_E & \cos T_E \end{bmatrix}. \tag{10}$$

We have then, recalling Eq. (4),

$$M_{12} M_{21} = 1 - M_{11} M_{22} = \sin^2 T_E . \tag{11}$$

Thus, a symmetrical multilayer is equivalent to a single homogeneous film with index of refraction N_E and thickness T_E defined by Eq. (9). When the matrix elements $|M_{11}|$, $|M_{22}| > 1$, the equivalent thickness is complex, and according to Eq. (8), steadily increasing matrix elements lead to steadily decreasing transmittance. We call the regions of imaginary equivalent index or complex equivalent thickness stop-bands. The other regions of real valued index and thickness are called pass-bands to the high transmittance.

Following Epstein[3] we used this concept as a powerful method to design multilayer films. A proper equivalent layer configuration is selected so that the stop-band covers the wavelength band in which low transmittance is required. If one equivalent layer system is not enough, several systems with different center wavelengths λ_c are used. The equivalent layer configurations are repeated until the proper low transmittance level is achieved. In regions where high transmittance is required, the pass-bands are placed and the various equivalent indices, the index of the substrate, and the index of the surrounding medium are matched either by making them equal to each other or by using internal antireflection coatings as matching layers.

The transmittance of a multilayer is a function of the optical thickness u_i $(i = 1, 2, \ldots, k)$ and the indices of refraction of the individual films n_i:

$$T = T(u_1, n_1; u_2, n_2; \ldots; u_k, n_k) . \tag{12}$$

By partial differentiation with respect to the u_i and n_i, we can relate changes of the optical thickness and indices of refraction to the resulting change in transmittance:

$$\Delta T \simeq \frac{\partial T}{\partial u_1}\Delta u_1 + \frac{\partial T}{\partial u_2}\Delta u_2 + \ldots + \frac{\partial T}{\partial u_k}\Delta u_k + \frac{\partial T}{\partial n_1}\Delta n_1 + \frac{\partial T}{\partial n_2}\Delta n_2 + \ldots + \frac{\partial T}{\partial n_k}\Delta n_k , \tag{13}$$

where T, ΔT and the partial derivatives are wavelength dependent.

The mathematical problems in carrying out the computations, though lengthy and tedious, are nevertheless straightforward. A. Thelen[4] and P. Baumeister[5] have calculated this refining method in detail. Consequently, it appears advisable to use the refining methods together with the design technique which takes the overall relations more into account. In our design process the equivalent layers are matched to each other, to the substrate, and to the medium. It is in this step where refining methods can be used to great advantage: one keeps the thickness of the equivalent layers constant and subjects the thickness of the matching layers to the refining process.

3. COATING OF THE THIN FILMS OF CRYOLITE AND CeO_2

The generally important properties of thin films are available in the literature for CeO_2[6] and Na_3AlF_6 (cryolite)[7,8]. Cryolite dissociates into NaF and AlF_3 during heating. The composition of the condensed films is dependent on boat temperature and evaporation rate. At low temperatures and low rates films that consist mainly of NaF are formed. At higher temperatures and rates mixed films of Na_3AlF_6 and NaF are condensed. Cryolite is transparent from 200 mμ up to 14 μ. The refractive index of cryolite films depends on the evaporation conditions and the resulting film composition. The refractive index of NaF films is 1.29–1.31, and that of AlF_3 films is 1.385. The refractive indices of cryolite films mentioned in the literature lie between 1.28 and 1.36.

CeO_2 is a widely used material for the production of high index films. CeO_2 films are transparent in the visible and infrared region up to 12 μ. The refractive index of CeO_2 films depends strongly on the substrate temperature T_s, and its value changes from 2.18 to

2.42 at 5,500 A^0 as T_s ranges from 50 to 350°C. CeO_2 films are very stable, hard and adhere well.

The coating system and the optical measurement system of our laboratory are well described in the literature by Chen and Wu[9]. The geometrical arrangement of the evaporation system is shown in Fig. 2.

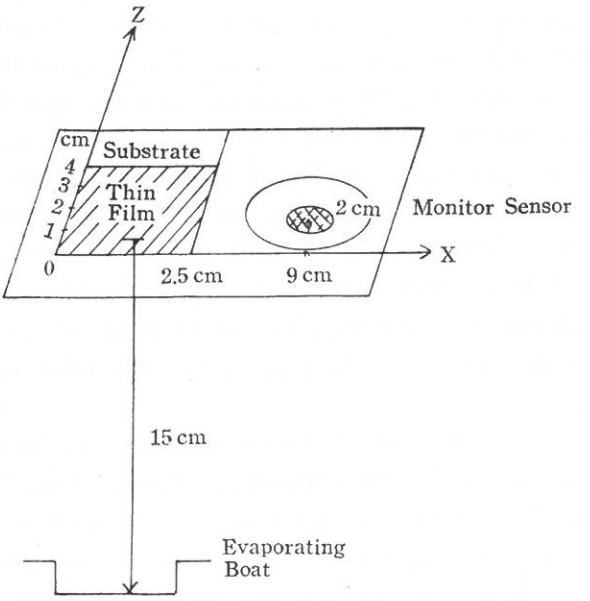

Fig. 2. The geometrical arrangement of the evaporation system. The monitor sensor is 2 cm above the substrate.

For the crystal film thickness monitor, the corresponding scaling numbers N for the materials to be deposited are calibrated by the inverse density and corrected for the vacuum system geometry. The actual thickness of deposited films is carefully measured by the Fizeau interference fringes method.[9] The thermal evaporation method is operated to heat CeO_2 and Na_3AlF_6. For the case of evaporation of CeO_2, an electrically heated tungsten boat which is connected to a 12 kw power supply is used. The evaporation power setting V(1, 5) supplies a voltage of 4.4 V and a current of 190 A to evaporate CeO_2 at the deposition rate of 15 A^0/sec at a vacuum

pressure of 5×10^{-5} Torr. The corrected material scaling number for CeO_2 is given as $N_{CeO_2} = 418$. A tantalum boat is used with power setting V(1, 3) which supplies a voltage of 2.3 V and a current of 110 A to evaporate cryolite at the deposition rate of 50 A°/sec at a vacuum pressure of 5×10^{-5} Torr. The material scaling number for cryolite is given as $N_{cryolite} = 556$.

The substrates are pyrex slides with refractive index $n_s = 1.512$ at room temperature. The substrate temperatures influence greatly the combination of CeO_2 and cryolite. We find, keeping the substrate temperature at 70°C that the combination of these two films shows the greatest stability, adhesion, and no fissures in the films are formed. The thickness of condensed films also depends on the substrate temperatures. For cryolite, the relative thickness according to a reading of 3,000 A° are 1.223, 1.030, 0.974 and 0.806 at substrate temperatures 140°C, 100°C, 70°C, and 50°C, respectively. Hence, in the experiments, we first bake the substrate up to 150°C, and then let it gradually cool down, keeping it at 70°C when the films are deposited.

The geometrical relation between evaporating source S and receiving surface *da* on the substrate is shown in Fig. 3. Consider the dose (CeO_2 or cryolite) on the boat as a small area *ds* from which material is evaporated at the rate of m gm/sec on to a parallel plane surface (substrate). The relative thickness distribution t/t_0 at R follows from Holland[10],

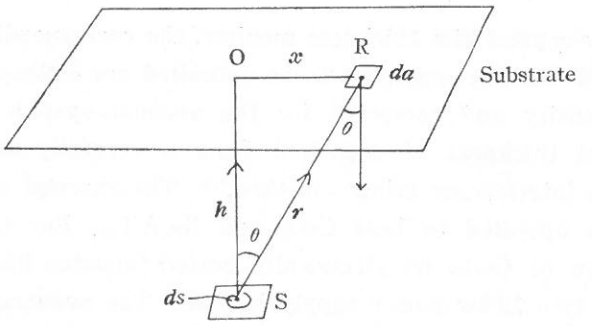

Fig. 3. The geometrical relation between evaporating source S and receiving surface *da* on the substrate.

$$\frac{t}{t_0} = \frac{1}{[1 + (x/h)^2]^2} \tag{14}$$

where t_0 is the thickness of the deposit just above the source, and h is the distance between the source and the substrate at the normal direction. r is the distance from the source to the receiving surface da at R, and x is the distance on the substrate from the point O which is directly above the source to the receiving surface at R.

Figure 4 shows the thickness distributions of deposit of CeO_2 and Na_3AlF_6 along with the theoretical prediction according to Eq. (14).

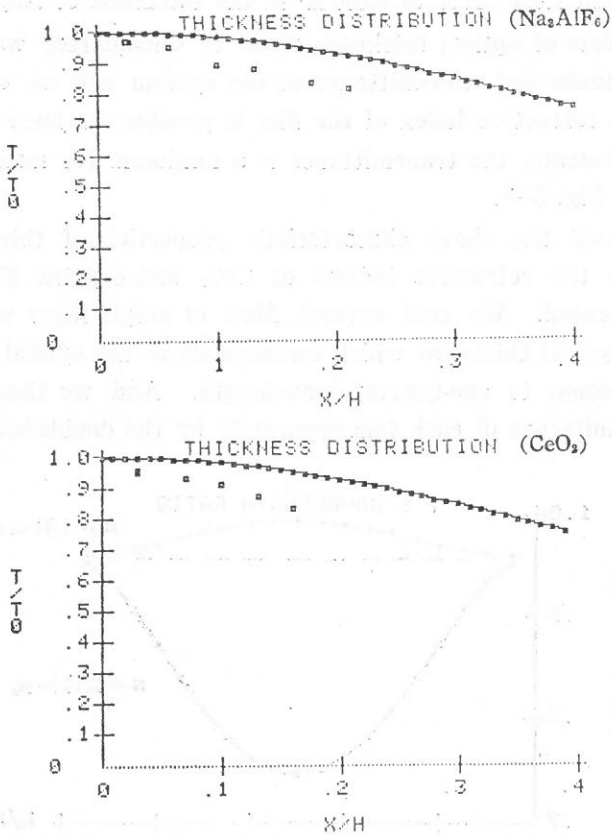

Fig. 4. The relative thickness distributions of deposit of CeO_2 and Na_3AlF_6 from experimental measuring (dots) and theoretical prediction (full line).

Here, from Fig. 2, h is 15 cm, so that the film thickness is maximum in the central 1 cm range because it is directly above the source, and then decreases to both ends. Therefore, when we measure the transmittance of the film, we just let the light pass through the central 1 cm range of the film.

In determining the film thickness by the optical interference method, the observed Fizeau fringes drift in time, and that causes errors in measuring the separation of fringes and the displacement of the fringe across the step which is used to determine the film thickness. The results are 3.5% error at 4,000 A^0 in the thickness of CeO_2, and 1.6% error at 5,000 A^0 in the thickness of Na_3AlF_6.

For films of optical thickness equal to one-quarter wavelength, the reflectance and transmittance of the system are an extremum. When the refractive index of the film is greater (or less) than that of the substrate, the transmittance is a minimum (or maximum) as shown in Fig. 5[11].

We used the above characteristic properties of thin films to determine the refractive indices of CeO_2 and cryolite films which we evaporated. We coat several films of single layer with a different physical thickness which corresponds to the optical thickness near or equal to one-quarter wavelength. And we then measure the transmittance of each film separately by the double beam optical

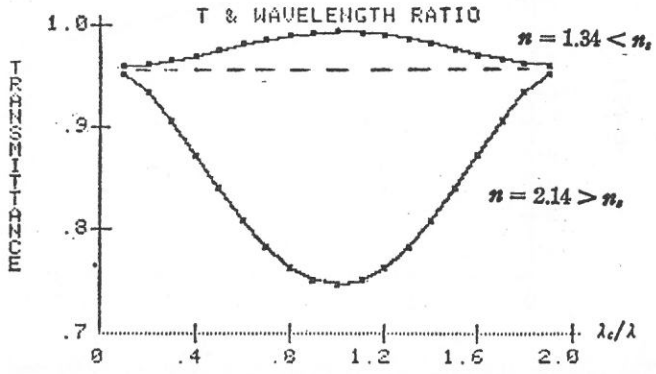

Fig. 5. Variation of transmittance with wavelength ratio of λ_c/λ at two different refractive indices 1.34 and 2.14.

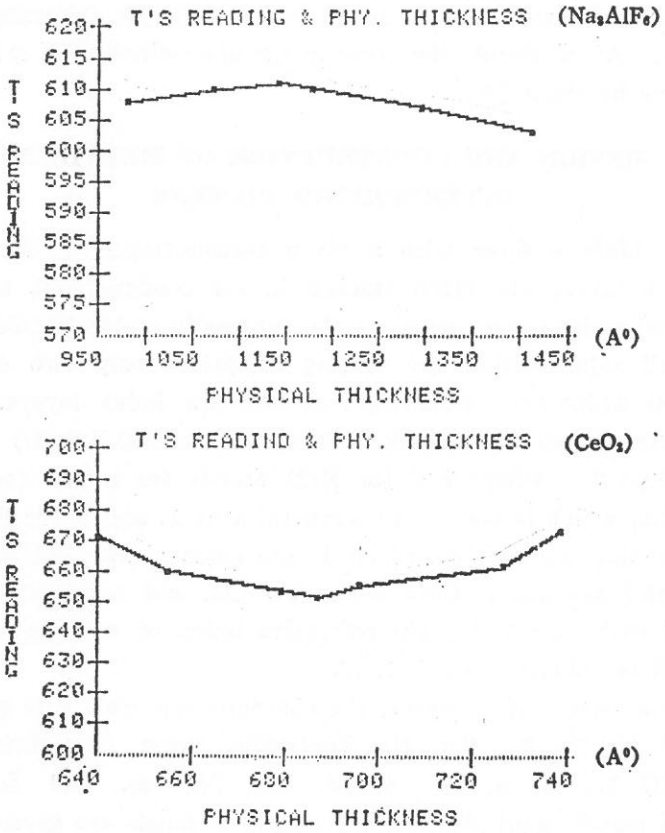

Fig. 6. Variation of transmittance reading with coated physical thickness of CeO_2 and Na_3AlF_6.

system[9]. The results are shown in Fig. 6. And from that we obtain that the transmittance of CeO_2 is minimum at a physical thickness $t = 687\ A^0$ which corresponds to the optical thickness $nt = \lambda/4$, where λ is the wavelength of sodium spectral light source at 5,890 A^0. Therefore, we conclude the refractive index of CeO_2 is 2.14. Similarly, for cryolite, the transmittance is maximum at $t = 1{,}098\ A^0$, and the refractive index $N_{Na_3AlF_6}$ is 1.34.

Due to the instability of electric voltage the error in the transmittance reading arising from the light detector can be 0.1–0.2%. This small error in transmittance could lead to the fluctuation in

physical thickness as large as 55 A^0 for CeO_2 by following Mouchart[12]. As a result, the error in the determination of refractive index can be about 7%.

4. DESIGN AND CONSTRUCTION OF MULTILAYER INTERFERENCE FILTERS

To obtain a filter with a given transmittance T, for wavelength λ, layers are often stacked in $\lambda/4$ configuration, since we know that under these conditions the process is stable ($\partial R/\partial\phi=0$)[12]. We shall suppose that the coating comprises only two different materials which are alternating high and low index layers. Here, we use two types of equivalent layers: I. ((L/2) H(L/2)) and II. ((H/2) L(H/2)), where L/2 (or H/2) stands for a low (or high)-index film which is one-eighth wave thick at λ_c and L (or H) for a low (or high)-index film which is one-quarter wave thick at λ_c. The high-index film is CeO_2 with $n_H = 2.14$, and low-index film is cryolite with $n_L = 1.34$. The refractive index of medium n_M is 1, and that of substrate n_S is 1.512.

For a stack of 3 layers, the characteristic matrix is given by Eq. (6) as N = 3. For the equivalent layer (H/2) L(H/2) or (L/2) H(L/2), let $n_1 = n_3$, $\phi_1 = \phi_3$ and $2\phi_1 = \phi_2$, and following straight matrix multiplication the matrix elements are given by

$$M_{11} = \cos 2\phi_1 \cos\phi_2 - \frac{1}{2}\left(\frac{n_2}{n_1} + \frac{n_1}{n_2}\right)\sin 2\phi_1 \sin\phi_2 ,$$

$$M_{12} = \frac{i}{n_1}\left[\sin 2\phi_1 \cos\phi_2 + \frac{1}{2}\left(\frac{n_1}{n_2} + \frac{n_2}{n_1}\right)\cos 2\phi_1 \sin\phi_2 + \frac{1}{2}\left(\frac{n_1}{n_2} - \frac{n_2}{n_1}\right)\sin\phi_2\right],$$

$$M_{21} = in_1\left[\sin 2\phi_1 \cos\phi_2 + \frac{1}{2}\left(\frac{n_1}{n_2} + \frac{n_2}{n_1}\right)\cos 2\phi_1 \sin\phi_2 - \frac{1}{2}\left(\frac{n_1}{n_2} - \frac{n_2}{n_1}\right)\sin\phi_2\right],$$

$$M_{22} = M_{11} .$$

From Eqs. (9) and (15), we use the computer to calculate equivalent indices N_E for the systems (L/2) H(L/2) and (H/2) L(H/2)

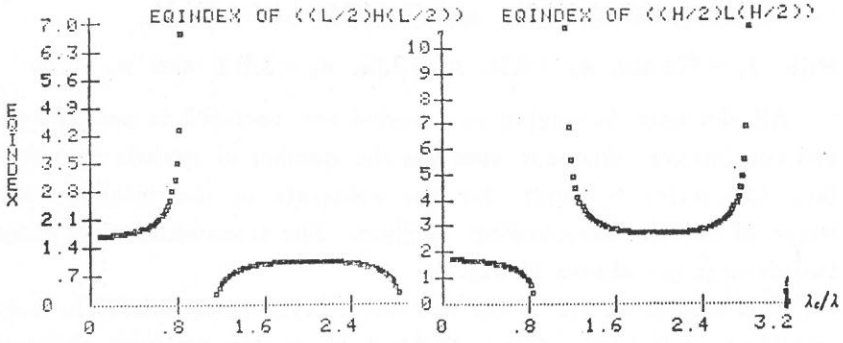

Fig. 7. Variation of equivalent index with wavelength ratio of λ_c/λ for equivalent layers (L/2)H(L/2) and (H/2)L(H/2).

in terms of λ_c/λ, where λ_c is the center wavelength of equivalent layer, and λ is the incident wavelength. The results are shown in Fig. 7. The computer programming for applesoft basic language is expressed in the appendix.

From Fig. 7, we find that the stop-band of these two equivalent layers lie in the same region of λ_c/λ, between 0.852 and 1.148. If we want to design a 500 mμ low-pass filter, let λ=500 mμ in the equation $\lambda_c/\lambda = 1.148$, we then obtain $\lambda_c = 574$ mμ. Also, put λ_c in $\lambda_c/\lambda = 0.852$ to get $\lambda = 674$ mμ. It means that if we pick $\lambda_c = 574$ mμ as the center wavelength of equivalent layers I and II, their stop-bands extend from 500 to 674 mμ, letting wavelengths less than 500 mμ transmit.

Here, we only want to compare the ability of transmission of the (L/2) H(L/2) layer with the (H/2) L(H/2) layer, and so we skip the mismatch problem between two indices with intervening antireflection coating, until we go to discuss band-pass filters later. The only thing remaining to be determined is the number of periods of the equivalent layer to be used. This number should be large enough to give a sufficiently high reflectance where required, but it should be small enough for simplicity of manufacture. Thus, we select 5 periods of layer I or II to allow the transmittance to be less than 10% in the stop-band, which results in the following designs:

$$S\,|[(L/2)\,H(L/2)]^5|\,M, \quad \text{and} \quad S|[(H/2)\,L(H/2)]^5|\,M,$$

with $\lambda_c = 574\ \mathrm{m}\mu$, $n_H = 2.14$, $n_L = 1.34$, $n_S = 1.512$, and $n_M = 1.0$.

All elements belonging to a period are enclosed in parentheses and the integer exponent specifies the number of periods in a design. The letter S stands for the substrate of the filter and the letter M for the surrounding medium. The transmittance of these two designs are shown in Fig. 8.

Obviously from Fig. 8, the equivalent layer (L/2) H(L/2) is more suitable to a low-pass filter. Table 1 shows the designed physical

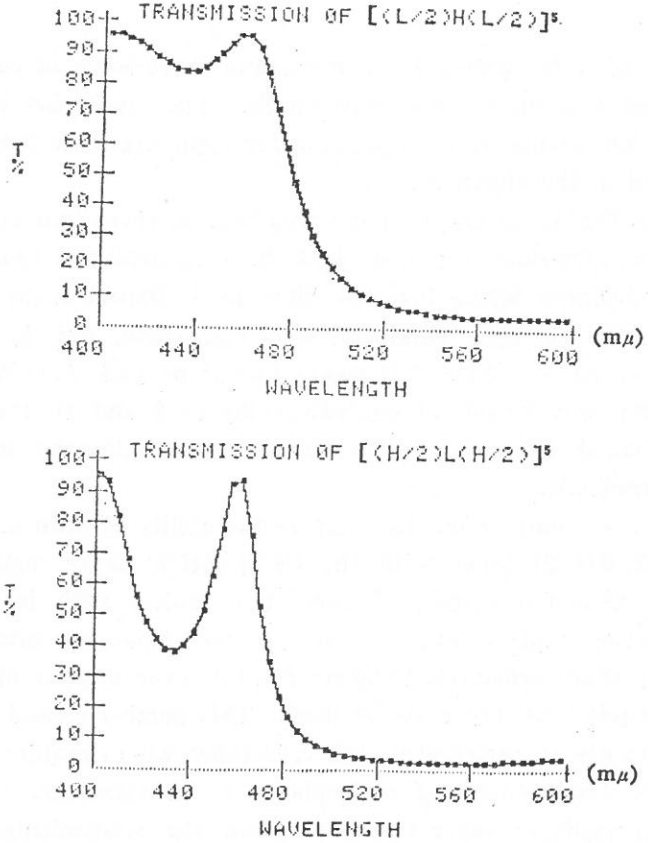

Fig. 8. Variation of transmittance with wavelength for equivalent layers $[(L/2)H(L/2)]^5$ and $[(H/2)L(H/2)]^5$.

thickness and the true coated thickness of 5 periods of the (L/2) H(L/2) layer for a low-pass filter. The corresponding computed transmittance to both thicknesses and the experimental measured value of transmittance are shown in Fig. 9.

Table 1. Optical description of the design S |[(L/2) H(L/2)]^5| M shown in Fig. 9

Layer	Index	Design thickness (A^0)	True coated thickness (A^0)
1	1.34	537	594
2	2.14	672	686
3	1.34	1,074	1,056
4	2.14	672	680
5	1.34	1,074	1,071
6	2.14	672	677
7	1.34	1,074	1,179
8	2.14	672	666
9	1.34	1,074	1,246
10	2.14	672	674
11	1.34	537	658

Note: The layers are counted from the medium.

Next, we design a 685 mμ high-pass filter. Let $\lambda = 685$ mμ in $\lambda_c/\lambda = 0.852$, and we obtain $\lambda_c = 584$ mμ. Also, put λ_c in $\lambda_c/\lambda = 1.148$ to get $\lambda = 509$ mμ. Thus, if we pick $\lambda_c = 584$ mμ as the center wavelength of equivalent layers I and II, their stop-bands extend from 509 to 685 mμ, letting wavelengths larger than 685 mμ transmit.

We also select 5 periods of layer I or II to allow the transmittance to be less than 10% in the stop-band, which results in the following designs:

S |[(L/2)H(L/2)]^5| M, and S |[(H/2)L(H/2)]^5| M,

with $\lambda_c = 584$ mμ, $n_H = 2.14$, $n_L = 1.34$, $n_S = 1.512$, and $n_M = 1.0$.

The transmittance of these two designs are shown in Fig. 10.

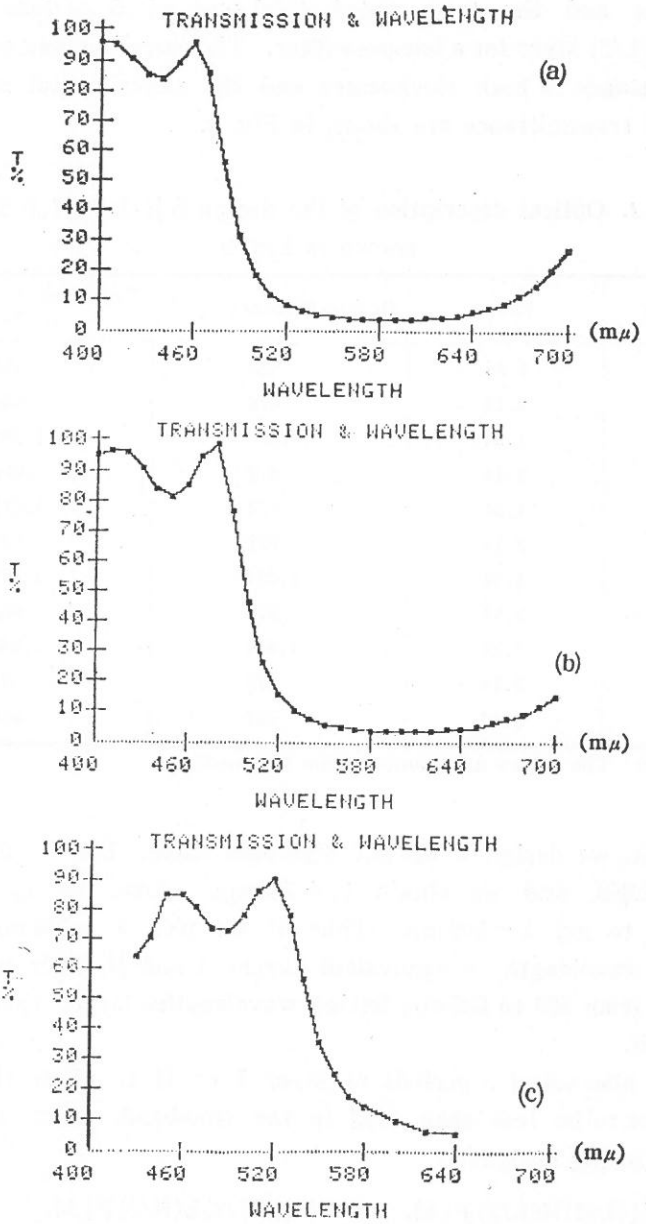

Fig. 9. The transmittance of the design given in Table 1. The computed transmittance corresponding to the designed thickness (column 3 of Table 1) is shown in (a), and to the coated thickness (column 4) is in (b). The measured transmittance is shown in (c).

Obviously from Fig. 10, the equivalent layer (H/2)L(H/2) is more effective to a high-pass filter. Table 2 shows the designed physical thickness and the true coated thickness of 5 periods of the (H/2)L(H/2) layer for a high-pass filter. The corresponding computed transmittance to both thicknesses and the experimental measured value of transmittance are shown in Fig. 11.

Finally, we design a band-pass filter with the desired pass-band extending from 490 to 580 mμ. Using the (L/2)H(L/2) layer as low-pass filter, we let $\lambda = 580$ mμ in $\lambda_c/\lambda = 1.148$ to give $\lambda_c = 665.8$ mμ, and we then put λ_c in $\lambda_c/\lambda = 0.852$ to get $\lambda = 781.5$ mμ. Thus, if

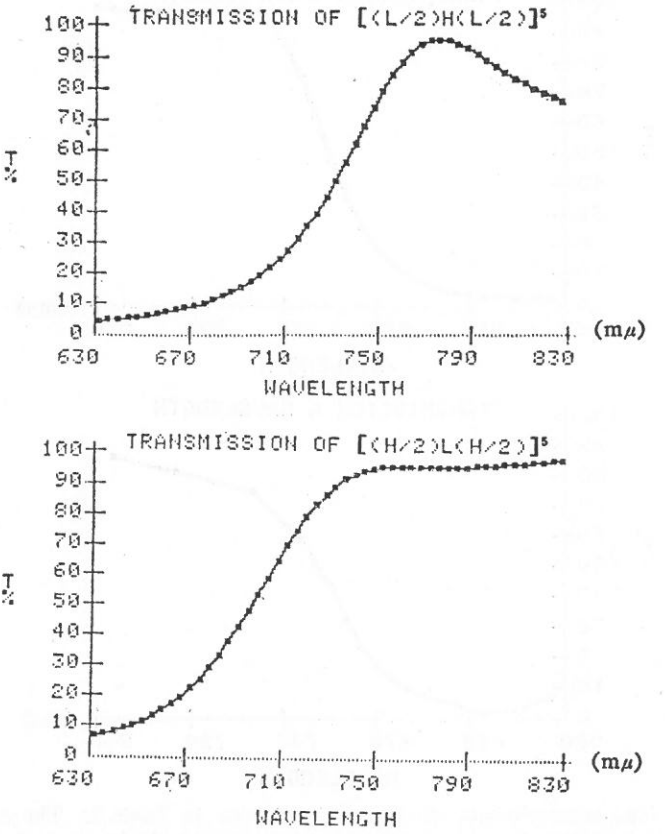

Fig. 10. Variation of transmittance with wavelength for equivalent layers $[(L/2)H(L/2)]^5$ and $[(H/2)L(H/2)]^5$.

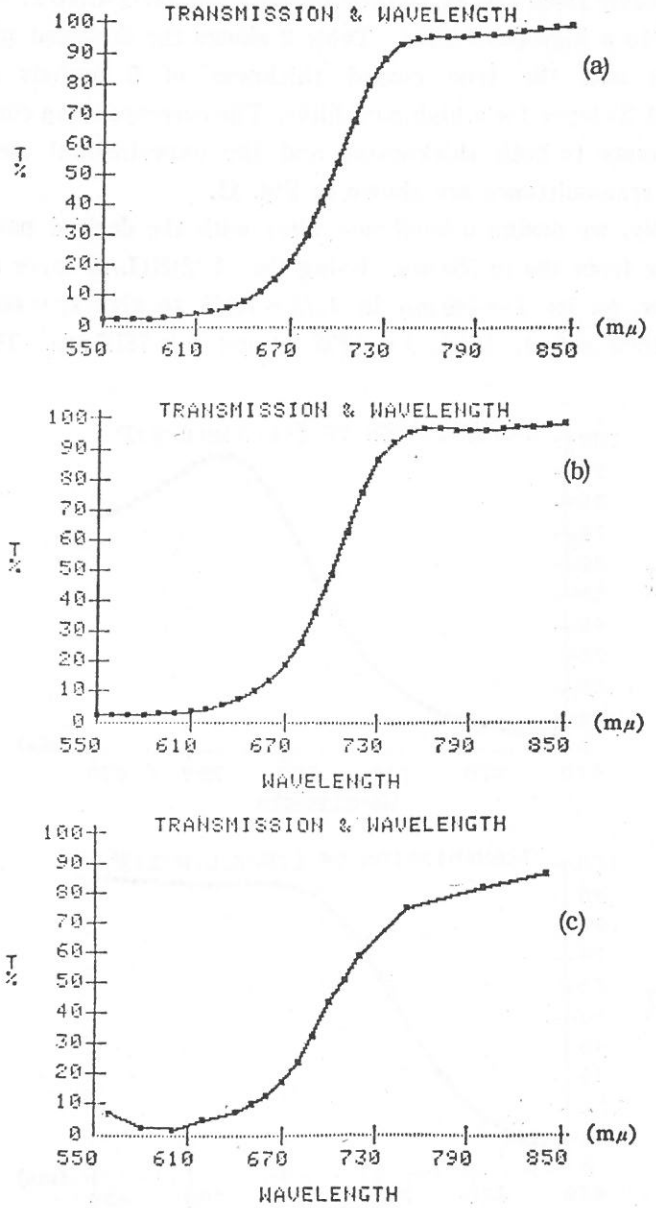

Fig. 11. The transmittance of the design given in Table 2. The computed transmittance corresponding to the designed thickness (column 3 of Table 2) is shown in (a), and to the coated thickness (column 4) is in (b). The measured transmittance is shown in (c).

Table 2. Optical description of the design S |[(H/2) L(H/2)]^5|M shown in Fig. 11

Layer	Index	Design thickness (A^0)	True coated thickness (A^0)
1	2.14	341	360
2	1.34	1,089	1,091
3	2.14	682	695
4	1.34	1,089	1,057
5	2.14	682	696
6	1.34	1,089	1,129
7	2.14	682	685
8	1.34	1,089	1,073
9	2.14	682	697
10	1.34	1,089	1,040
11	2.14	341	348

Note: The layers are counted from the medium.

we pick $\lambda_c = 665.8\,\mathrm{m}\mu$ as the center wavelength of the equivalent layer (L/2)H(L/2), its stop-band extends from 580 to 781.5 mμ. On the other hand, using the (H/2)L(H/2) layer as high-pass filter, we let $\lambda = 490\,\mathrm{m}\mu$ in $\lambda_c/\lambda = 0.852$ to give $\lambda_c = 417.5\,\mathrm{m}\mu$, and we then put λ_c in $\lambda_c/\lambda = 1.148$ to get $\lambda = 363.6\,\mathrm{m}\mu$. Thus, if we pick $\lambda_c = 417.5\,\mathrm{m}\mu$ for the equivalent layer (H/2)L(H/2), its stop-band extends from 363.6 to 490 mμ. Therefore, the gap between these two stop-bands forms the desired pass-band extending from 490 to 580 mμ.

Now, we have to consider the match between the various equivalent indices, the index of the substrate, and the index of the surrounding medium by making them equal to each other or by using internal antireflection coatings as matching layers. Fig. 12 shows the equivalent indices of (L/2)H(L/2) and (H/2)L(H/2) layers between the wavelength of 490 to 580 mμ.

From Fig. 12, the indices of these two layers are equal at 516 mμ. At other wavelengths, the mismatch between these two indices varies so rapidly that it would be very hard to find a

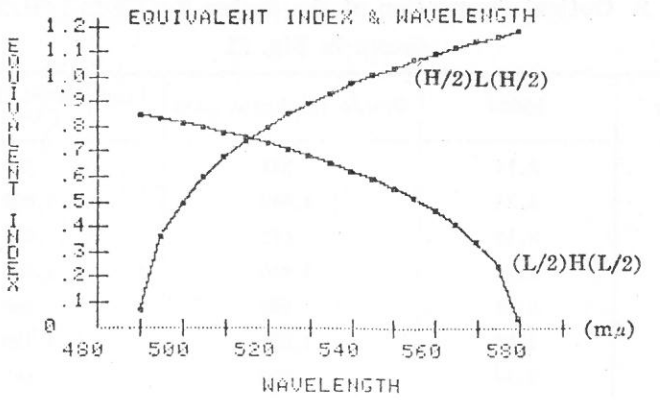

Fig. 12. Variation of the equivalent index with wavelength between 490 and 580 mμ for layers (L/2)H(L/2) and (H/2)L(H/2).

satisfactory antireflection coating between them. Accordingly, the junction between these two (H/2)L(H/2) and (L/2)H(L/2) layers does not need antireflection coating. Also, the equivalent index of the (H/2)L(H/2) layer equals that of air ($n = 1$) at 544 mμ. Similarly, the (H/2)L(H/2) layer is placed in contact with air without an intervening antireflection coating.

The (L/2)H(L/2) layer is placed on the substrate, but its equivalent index does not equal that of substrate ($n_s = 1.512$) anywhere between 490 and 580 mμ. Thus, the need of antireflection coating at the junction of (L/2)H(L/2) layer and substrate becomes unavoidable. Since the index of the (L/2)H(L/2) layer changes so rapidly with wavelength, a particular value is chosen as a compromise. If we choose the wavelength at 544 mμ, the corresponding equivalent index of the layer is 0.598. Then the index of the antireflection coating should be $(0.598 \times 1.512)^{1/2} = 0.950$, the geometric mean of this equivalent index 0.598 and index of substrate 1.512. In fact, it is not easy to find a substance having this particular value of refractive index 0.950. But this index is equal to the equivalent index of the (L/2)H(L/2) layer at $\lambda_c/\lambda = 1.49$. The center wavelength of this (L/2)H(L/2) layer is then $\lambda_c = 544 \times 1.49 = 810.6$ mμ. Consequently, we use as antireflection coating one

period of the (L/2)H(L/2) layer at $\lambda_c = 810.6\ \mathrm{m}\mu$.

Considering the simplicity of manufacture and sufficiency of high reflectance where required, we select four periods of each (L/2)H(L/2) and (H/2)L(H/2) layer which results in the following design:

$$S\ |1.485[(L/2)H(L/2)]^1,\ 1.219[(L/2)H(L/2)]^4,\ 0.765[(H/2)L(H/2)]^4|\ M,$$

with $\lambda_0 = 546\ \mathrm{m}\mu$, $n_H = 2.14$, $n_L = 1.34$, $n_S = 1.512$, and $n_M = 1.0$.

The factors associated with L and H in front of the paren-

Table 3. Optical description of the design of the band-pass filter shown in Fig. 13

Layer	Index	Design thickness (A°)	True coated thickness (A°)
1	2.14	244	238
2	1.34	778	787
3	2.14	488	487
4	1.34	778	808
5	2.14	488	494
6	1.34	778	806
7	2.14	488	486
8	1.34	778	803
9	2.14	244	230
10	1.34	621	657
11	2.14	778	772
12	1.34	1,242	1,302
13	2.14	778	785
14	1.34	1,242	1,182
15	2.14	778	775
16	1.34	1,242	1,282
17	2.14	778	779
18	1.34	1,375	1,329
19	2.14	944	923
20	1.34	754	714

Note: The layers are counted from the medium.

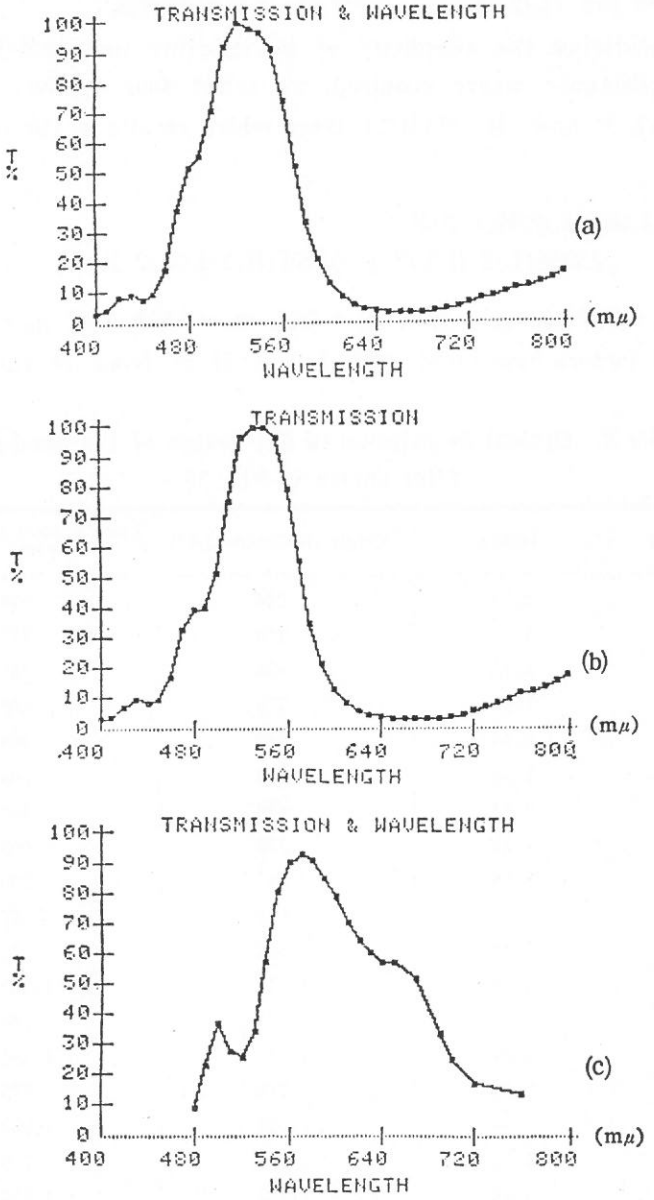

Fig. 13. The transmittance of the design given in Table 3. The computed transmittance corresponding to the designed thickness (column 3 of Table 3) is shown in (a), and to the coated thickness (column 4) is in (b). The measured transmittance is shown in (c).

thesis are equal to λ_c/λ_0 such that they change λ_0 into the desired center wavelength λ_c. And, from each center wavelength λ_c we can make a correspondence to the designed physical thickness of each layer of thin film in the stack.

Table 3 shows the designed physical thickness and true coated thickness of 4 periods of (H/2)L(H/2) layer, 4 periods of (L/2)H(L/2) layer, and 1 period of (L/2)H(L/2) as antireflection coating. The corresponding computed transmittance to both thicknesses, and the experimental measured value of transmittance are shown in Fig. 13.

Fig. 14 shows the computed transmittance of the same design of band-pass filter as above except without the antireflection coating layer. Comparing Fig. 13(a) with Fig. 14, we see that the adding of the antireflection coating layer increases the transmittance withjn the pass-band of filters with significant effects. And we conclude that it is definitely needed in the above designs of interference filters with the combination of CeO_2 and cryolite.

5. DISCUSSIONS

In general, the transmittance curves of all three filters produced are compatible to the designed patterns. However, in more detailed

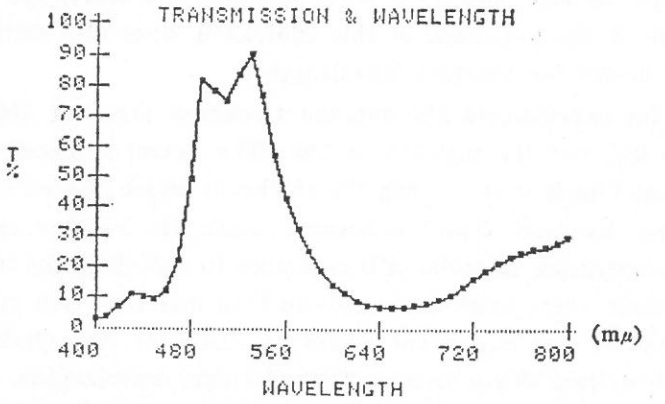

Fig. 14. The computed transmittance of the same design as Fig. 13 except without the antireflection coating layer.

examination, we find the following discrepancies. The edge of the high-pass filter shifts only slightly toward longer wavelengths, but its slope becomes less steep, and so the transmittance in the considerable region of the high-pass side is lower than the desired value. The edge of the low-pass filter shifts significantly, about 40 mμ toward longer wavelengths, while its edge slope and transmittance are quite close to the design. The pass-band of the band-pass filter expands and shifts considerably toward longer wavelengths.

These discrepancies may come from the experimental error in determining the refractive indices n_L and n_H as well as the thickness of thin films during the coating process.

A systematic error in under (or over) estimation of the physical thickness of every layer has the effect equivalent to changing the center wavelength λ_c of the equivalent layers, and so making the transmittance curve shift toward longer (or shorter) wavelengths. We estimate that when the physical thickness in each (H/2) layer of the equivalent layer (H/2)L(H/2) increases (or decreases) by 23A^0 and its L layer increases (or decreases) by 74A^0, the edge of the pass-band of this equivalent layer shifts 40 mμ toward longer (or shorter) wavelengths. And when the physical thickness in each (L/2) layer of the equivalent layer (L/2)H(L/2) increases (or decreases) by 38A^0 and its H layer increases (or decreases) by 42A^0, the edge of the pass-band of this equivalent layer also shifts 40 mμ toward longer (or shorter) wavelengths.

In the experiments, the average thickness error at 1000A^0 for CeO_2 is 9%, and for cryolite is 3%. The actual thickness of the deposited film is greater than the thickness which is read from the thickness monitor. This is because when the shutter is closed, some evaporating material still continues to deposit on the substrate. As a result, these thickness errors in both materials will cause the pass-band of both equivalent layers (L/2)H(L/2) and (H/2)L(H/2) to shift at least 40 mμ or more toward longer wavelengths. At the same time, these thickness errors in both materials will cause to change the values of their respective refractive index which is

determined by the variation of transmittance with thickness as mentioned in section 3. The actual refractive index can be 2.0 instead of 2.14 for CeO_2 responding to the 9% error in thickness, and 1.31 instead of 1.34 for cryolite responding to the 3% error in thickness.

The influences of errors in refractive indices are examined by the computer analysis of the variations of the pass-band and its edges in the equivalent index curve with respect to changes of n_L and n_H. For the (L/2)H(L/2) layer used in the low-pass filter, a decrease (or an increase) in n_H or an increase (or a decrease) in n_L will shift the edge of the pass-band toward longer (or shorter) wavelengths. For the (H/2)L(H/2) layer used in the high-pass filter, an increase (or a decrease) in n_H or a decrease (or an increase) in n_L will shift the edge of the pass-band toward longer (or shorter) wavelengths.

Taking the refractive indices as $n_H = 2.0$ and $n_L = 1.31$ which are due to the thickness errors as above, the edge of the low-pass filter shifts neither toward longer nor toward shorter wavelengths. But, these thickness errors in both materials of the (L/2)H(L/2) layer cause a shift of 40 mμ toward longer wavelengths. As a result, the edge of the pass-band of the low-pass filter shifts 40 mμ toward longer wavelengths, the same as shown in Fig. 9. On the other hand, the edge of the high-pass filter shifts about 30 mμ toward shorter wavelengths. Since the thickness error causes a shift of 40 mμ toward longer wavelengths, as a result, the edge of the pass-band of the high-pass filter shifts 10 mμ toward longer wavelengths, the same as shown in Fig. 11.

Fig. 15 shows the equivalent indices of layer (L/2)H(L/2) as a function of wavelength at different values of n_H and n_L for the band-pass filter between 490 and 580 mμ. And Fig. 16 shows the equivalent indices of layer (H/2)L(H/2) for the same band-pass filter. Taking the thickness error into account, we also choose $n_H = 2.0$ and $n_L = 1.31$. From Figs. 15(b) and (c), the edge of the pass-band of layer (L/2)H(L/2) shifts 20 mμ toward longer wavelengths, comparing with Fig. 15(a). And from Fig. 16(b) and (c),

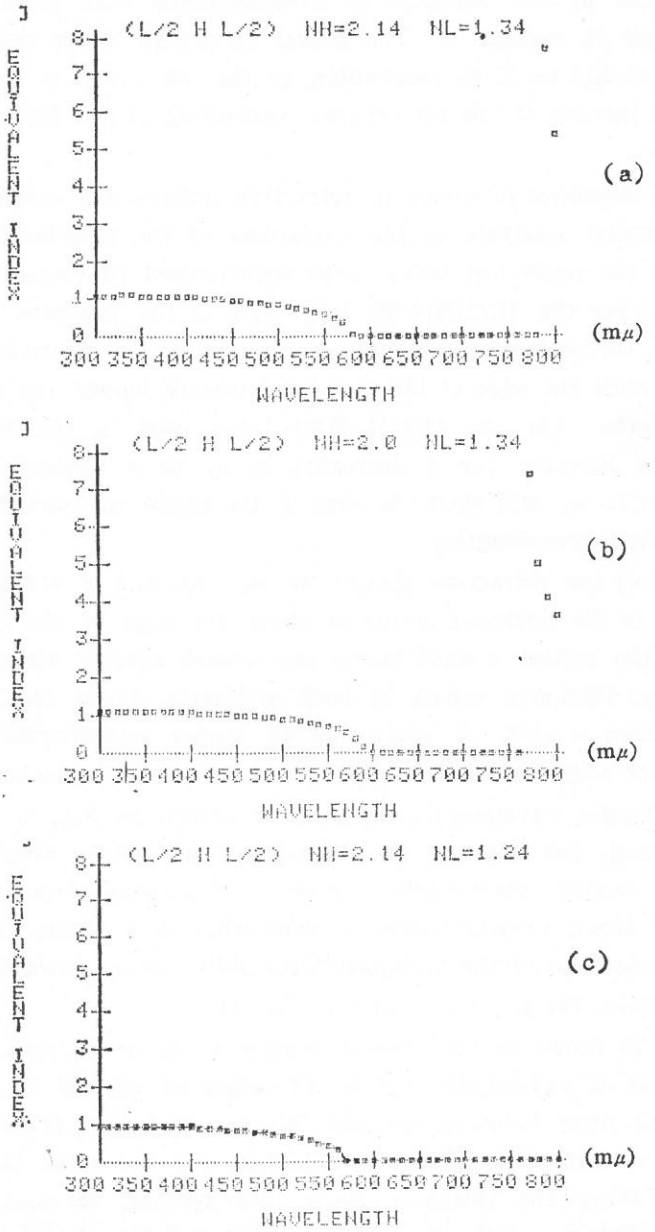

Fig. 15. Variation of equivalent index of layer (L/2)H(L/2) with wavelength at different n_L and n_H for the band-pass filter at wavelengths extending from 490 to 580 mμ.

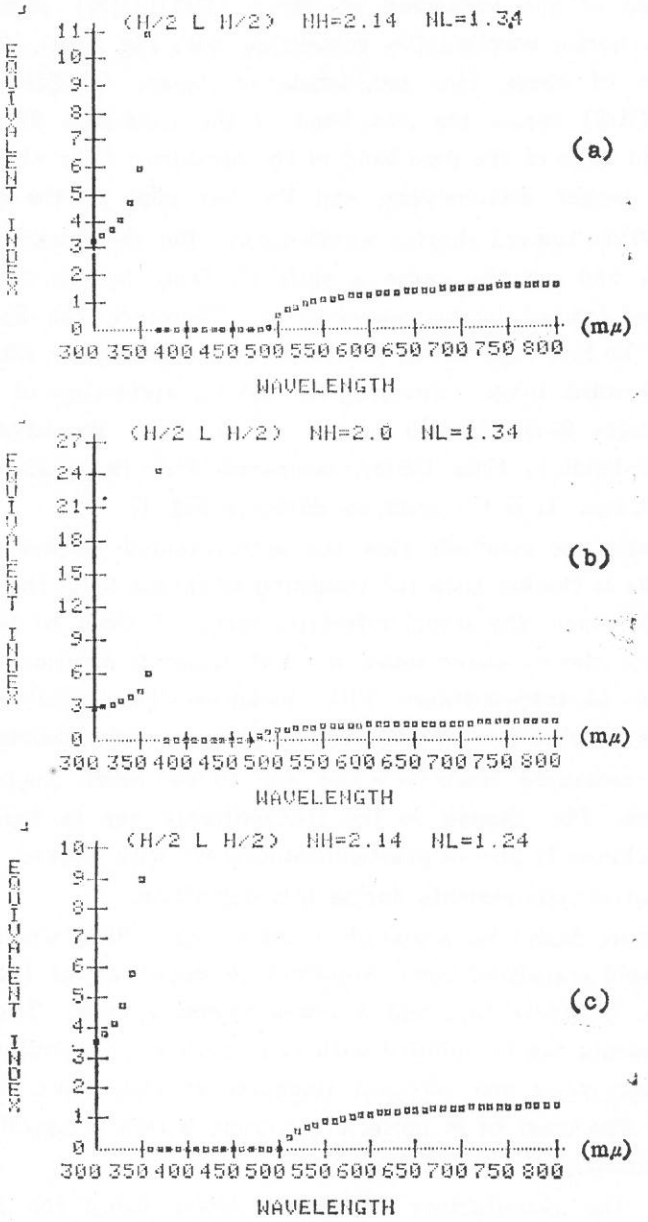

Fig. 16. Variation of equivalent index of layer (H/2)L(H/2) with wavelength at different n_L and n_H for the band-pass filter at wavelengths extending from 490 to 580 mμ.

the edge of the pass-band of layer (H/2)L(H/2) shifts 20 mμ toward shorter wavelengths, comparing with Fig. 16(a). The combination of these two pass-bands of layers (L/2)H(L/2) and (H/2)L(H/2) forms the pass-band of the band-pass filter. Thus, the right edge of the pass-band of the band-pass filter shifts 20 mμ toward longer wavelengths, and the left edge of the pass-band shifts 20 mμ toward shorter wavelengths. But the thickness errors in CeO_2 and cryolite cause a shift of 40 mμ in the edge of the pass-band toward longer wavelengths. Therefore, the final result is that the left edge of the pass-band of the band-pass filter shifts 20 mμ toward longer wavelengths, and the right edge of the pass-band shifts 60 mμ toward longer wavelengths. The bandwidth of the pass-band is then 150 mμ compared with the designed bandwidth 90 mμ. It is the same as shown in Fig. 13.

Finally, we conclude that the actual coated thickness on the substrate is thicker than the measured thickness from the monitor. And this causes the actual refractive index of CeO_2 to be always less than the measured index $n = 2.14$ which is determined by the variation of transmittance with thickness. The actual refractive index of cryolite is only slightly less than or approximately equal to the measured index $n = 1.34$ due to the small fluctuation of thickness. The change in the transmittance due to variation in film thickness is also of practical importance with regard to thickness control requirements during film deposition.

A more desireable shape of an interference filter would show a more rapid transition from stop-band to pass-band at the desired position, a flatter top, and a lower rejection level. These three requirements can be fulfilled with more accurate determinations of refractive index and physical thickness of thin films. The evaporated film must be of uniform thickness within a specified area, and accurately controlled during evaporation.

But the manufacture of optical filters using the thin film technique is not easy, since the problem of process reproducibility frequently arises. The essential causes of existing problems arise firstly from the use of evaporation products, the indices of which

fluctuate according to deposition conditions, and secondly from the methods used for testing deposit thicknesses, these methods not being sufficiently accurate.

REFERENCES

(1) Abelès, F., *Ann. Phys.* 5, 596, 706 (1950).
(2) Born, M. and Wolf, E., "*Principles of Optics*", 6th ed., pp. 36-70, Pergamon Press, Oxford (1980).
(3) Epstein, L. I., *J. Opt. Soc. Am.* 42, 806 (1952).
(4) Thelen, Alfred, "*Physics of Thin Films*", vol. 5, pp. 68-85, Academic Press, New York (1969).
(5) Baumeister, Philip, *J. Opt. Soc. Am.* 48, 955 (1958).
(6) Hass, G., Ramsey, J. B., and Thun, R., *J. Opt. Soc. Am.* 48, 324 (1958).
(7) Ritter, Elmar, "*Physics of Thin Films*", Vol. 8, pp. 1-45, Academic Press, New York (1975).
(8) Heaven, O. S. and Smith, S. D., *J. Opt. Soc. Am.* 47, 469 (1957).
(9) Chen, J. I. and Wu, K. T., *Fu Jen Studies*, 15, 19 (1981), (Fu Jen University).
(10) Holland, L., "*Vacuum Deposition of Thin Films*", pp. 141-168, Chapman & Hall, London (1956).
(11) Heavens, O. S., "*Physics of Thin Films*", Vol. 2, pp. 193-237, Academic Press, New York (1964).
(12) Mouchart, Jacques, *Appl. Opt.*, 16, 2486 (1977).

APPENDIX

This is a computer program for the applesoft basic language used for calculating the variations of equivalent index and transmittance of filters with respect to wavelength.

```
10  REM  COMPUTE TRANSMITTANCE AND EQUIVALENT INDEX OF ANY EQUIVALENT LAY
     ER WITH RESPECT TO WAVELENGTH OR RATIO OF CENTER WAVELENGTH TO INCIDE
     NT WAVELENGTH
20  REM  FOR LAYER (L/2 H L/2),PUT IN NH:HIGH INDEX,NL:LOW INDEX.  FOR (H/
     2 L H/2),PUT IN NH:LOW INDEX, NL:HIGH INDEX.
30  REM  TAKE THE DENOMINATOR OF THE RATIO OF THICKNESS WITH EACH OTHER IN
      EVERY FILM AS THE VALUE OF THE "THICKNESS RATIO".
100  DIM A(2,2),B(2,2),C(2,2),D(4)
110  DIM T(100),N1(100),L1(100)
120 PI = 3.1415926
125  INPUT "INDEX OF SUBSTRATE ";FS
126  INPUT "INDEX OF MEDIUM ";FO
140  INPUT "DO YOU GIVE CENTRAL WAVE RATIO (Y&N) ";E$
150  INPUT "RANGE OF FILTERING WAVELENGTH ";LS,LF
160  PRINT
170  INPUT "STEP WIDTH";ST
180  INPUT "CONTAIN HOW MANY KINDS OF STACKS ";WHOLE
190  FOR G = 1 TO WHOLE
200  INPUT "NO. OF FILMS ";F1(G)
210  INPUT "NO. OF STACK ";F(G)
220  INPUT "INDEX NH;NL ";XH(G),XL(G)
230  FOR E = 1 TO F1(G)
240  INPUT "THICKNESS RATIO ";Y(G,E)
250  NEXT E
260  IF E$ = "Y" THEN GOTO 280
270  INPUT "CENTRAL WAVELENGTH ";LC(G)
280  NEXT G
290  INPUT "PRINT OUT OR NOT?";A1$
300  IF A1$ <  > "Y" THEN 340
330  PRINT  CHR$ (4);"PR#1"; CHR$ (13)
340 QQ = 0
410  FOR LM = LS TO LF STEP ST
420  FOR H = 1 TO WHOLE
430 B1(H) = F1(H):BO(H) = F(H)
440 NH(H) = XH(H):NL(H) = XL(H)
450  FOR D = 1 TO B1(H)
460 X(H,D) = Y(H,D)
470  NEXT D
480  IF E$ = "Y" THEN  GOTO 520
490 LZ(H) = LC(H)
500 ALFA = 0.5 * PI * LZ(H) * (1 / LM)
510  GOTO 530
520 ALFA = 0.5 * PI * LM
530  FOR I = 1 TO BO(H)
```

```
540  FOR J = 1 TO B1(H)
550  IF J <  > 1 OR I <  > 1 OR H <  > 1 THEN  GOTO 610
560 B(1,1) =  COS (ALFA / X(H,J))
570 B(1,2) = (1 / NL(H)) *  SIN (ALFA / X(H,J))
580 B(2,1) = NL(H) *  SIN (ALFA / X(H,J))
590 B(2,2) = B(1,1)
592  IF B1(H) = 1 THEN  GOTO 1140
600  GOTO 800
610  IF  INT (J / 2) <  > J / 2 THEN  GOTO 670
620 A(1,1) =  COS (ALFA / X(H,J))
630 A(1,2) = (1 / NH(H)) *  SIN (ALFA / X(H,J))
640 A(2,1) = NH(H) *  SIN (ALFA / X(H,J))
650 A(2,2) = A(1,1)
660  GOTO 710
670 A(1,1) =  COS (ALFA / X(H,J))
680 A(1,2) = (1 / NL(H)) *  SIN (ALFA / X(H,J))
690 A(2,1) = NL(H) *  SIN (ALFA / X(H,J))
700 A(2,2) = A(1,1)
710 C(1,1) = A(1,1) * B(1,1) - A(1,2) * B(2,1)
720 C(1,2) = A(1,1) * B(1,2) + A(1,2) * B(2,2)
730 C(2,1) = A(2,1) * B(1,1) + A(2,2) * B(2,1)
740 C(2,2) = A(2,2) * B(2,2) - A(2,1) * B(1,2)
750  FOR K = 1 TO 2
760  FOR L = 1 TO 2
770 B(K,L) = C(K,L)
780  NEXT L
790  NEXT K
800  NEXT J
810  NEXT I
820  NEXT H
860 D(1) = C(1,1)
870 D(2) = C(1,2)
880 D(3) = C(2,1)
890 D(4) = C(2,2)
900 U = PO / PS
910 V = PO * PS
920 W = 2 + U * (D(1)) ^ 2
930 F = (1 / U) * (D(4)) ^ 2
940 G = V * (D(2)) ^ 2
950 H = (1 / V) * (D(3)) ^ 2
955 QQ = QQ + 1
960 T(QQ) = 4 / (W + F + G + H)
965 L1(QQ) = LM
980  PRINT L1(QQ),"TRANSMISSION=";T(QQ)
1020 NI = C(2,1) / C(1,2)
1030  IF NI < 0 THEN  GOTO 1090
1040 N1(QQ) = NI ^ (1 / 2)
1060  PRINT L1(QQ),"EQINDEX=";N1(QQ)
1070  PRINT : PRINT
1090  NEXT LM
```

```
1110  PRINT  CHR$ (4);"PR#0"; CHR$ (13)
1111  FOR J = 1 TO 2
1112  IF J = 2 THEN 1115
1113  INPUT "TRANSMISSION FILE NAME.";A$
1114  GOTO 1116
1115  INPUT "EQINDEX FILE NAME.";A$
1116  PRINT  CHR$ (4);"OPEN";A$
1117  PRINT  CHR$ (4);"WRITE";A$
1118  PRINT 100
1119  PRINT 100
1120  FOR LM = 1 TO 00
1121  IF J = 2 THEN 1124
1122  PRINT L1(LM): PRINT T(LM)
1123  NEXT LM: GOTO 1126
1124  PRINT L1(LM): PRINT N1(LM)
1125  NEXT LM
1126  PRINT  CHR$ (4);"CLOSE";A$
1127  NEXT J
1128  PRINT  CHR$ (4);"BLOAD CHAIN,A520"
1129  CALL 520"PLOT HELLO"
1130  END
1140  FOR K = 1 TO 2
1150  FOR L = 1 TO 2
1160 C(K,L) = B(K,L)
1170  NEXT L
1180  NEXT K
1190  GOTO 860
```

A STUDY OF THE ELECTRICAL RESISTIVITY OF LIQUID TIN*

HSUEH-TAU CHOU, TAI-SONE YIH
and SHEAU-HUEY CHIA

ABSTRACT

We used a simple four-probe method to measure the electrical resistivity of Liquid Tin as a function of temperature. Our measurements were then compared with the results obtained from Ziman's theory by numerically integrating the data from X-ray diffraction and neutron scattering experiments for structure factors with various pseudopotential models. The Ziman theory was seen to be compatible with our measurements.

I. INTRODUCTION

It is by now more than two decades since Ziman proposed his theory of electrical conductivity for simple liquid metals with nearly free electrons.[1] He found that the electrical resistivity ρ depends critically on two functions which describe the physical behavior of the liquid metals. These functions are structure factor $S(\vec{q})$ and the pseudopotential $U(\vec{q})$. Interestingly enough, the past twenty years also saw many experimental activites[2] in measuring the structure factor of liquid metals by using both the X-ray diffraction and the neutron scattering techniques. And at nearly the same time, for some or other reasons, many theoretical models for the pseudopotential of the liquid metal were proposed.[3] These experimental and theoretical advancements would then allow us to make detailed studies of the Ziman's theory of electrical resistivity of simple liquid metals.

In this paper, we report the measured results of the electrical resistivity of liquid Tin as a function of temperature and then compare them with the theoretical values calculated from the Ziman theory with the data obtained in references (2) and (3). There are

* Supported by NSC grant, grant number NSC70-0204-M008-13

two reasons for us to do this work. Firstly, as far as we know, some one[4] may have calculated the electrical conductivity of liquid Tin from the Ziman theory at some particular temperature, no one[6] ever calculated the electrical resistivity of liquid Tin *as a function of temperature* by using the data given in references (2) and (3) for $S(\vec{q})$ and $U(\vec{q})$. Secondly, the measured temperature dependence of the electrical resistivity has not been clearly presented in literature.[5]

We shall devide the following discussions into three sections. In the first section we shall calculate the electrical resistivity of liquid Tin by integrating the data given in references (2) and (3) with the pseudopotentials of various models. The second section will deal with the experimental measurement of ρ. And we shall present our results and discussions in the last section.

II. MODEL CALCULATION OF THE RESISTIVITV OF LIQUID TIN

According to the Ziman's theory of the electrical resistivity simple liquid metals with nearly free electrons have their resistivity expressed as

$$\rho = \frac{3\pi m^{*2} \Omega_0}{4e^2 \hbar^3 k_F^6} \int_0^{2k_F} S(\vec{q}) \, |U(\vec{q})|^2 q^3 \, dq \qquad (1)$$

where m^* is the effective mass of the electron

Ω_0 is the atomic value

e is the electronic charge

$\hbar = \frac{h}{2\pi}$

k_F is the Fermi wave vector of nearly free electrons

$S(\vec{q})$ is the structure factor

$U(\vec{q})$ is the pseudopotential.

To calculate ρ by using the Ziman's formula, we shall use the experimental data for the structure factor of D. Jovic and

I. Padureanu as a case and that of D.M. North, J.E. Enduby and P.A. Egelstaff as another. These data on $S(\vec{q})$ will be integrated numerically with the pseudopotentials of the various known models. [3] The so calculated electrical resistivities of liquid Tin as a function of temperature are plotted in Fig. 1 and Fig. 2.

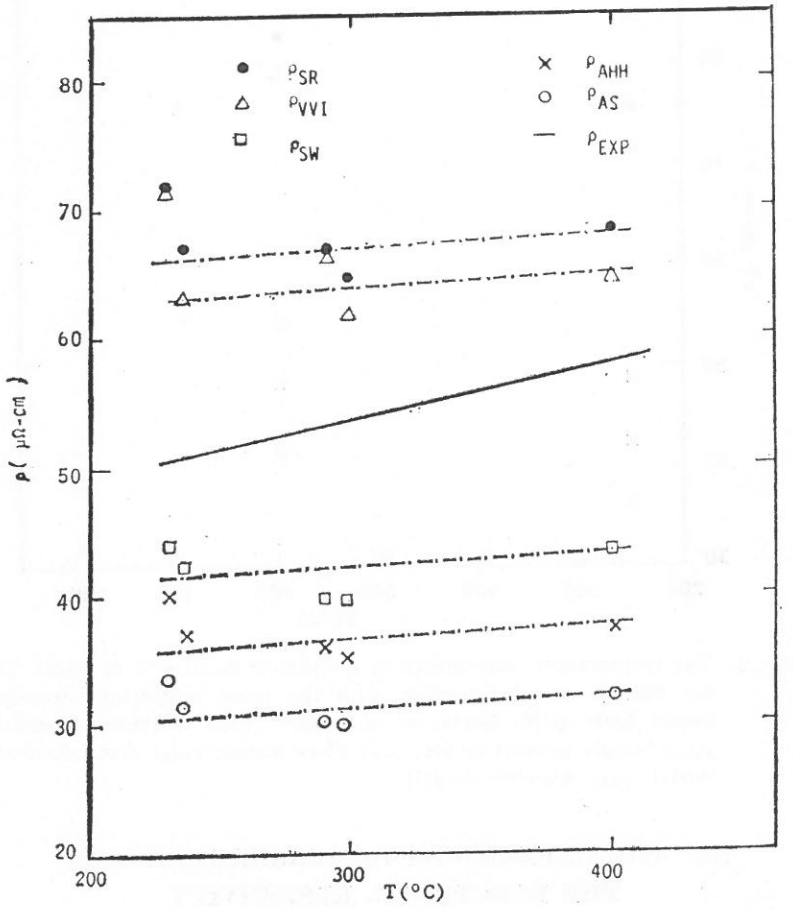

Fig. 1. The temperature dependence of the resistivity of liquid Tin for various pseudopotentials with the same scattering structure factor from D. Jovic, *et al.* 1976.[2] (ρ_{EXP}: Experimental; ρ_{SR}: Srivastava model; ρ_{VVI}: Simple general model; ρ_{SW}: Shaw model; ρ_{AHH}: Animalu-Heine model; ρ_{AS}: Ashcroft model)

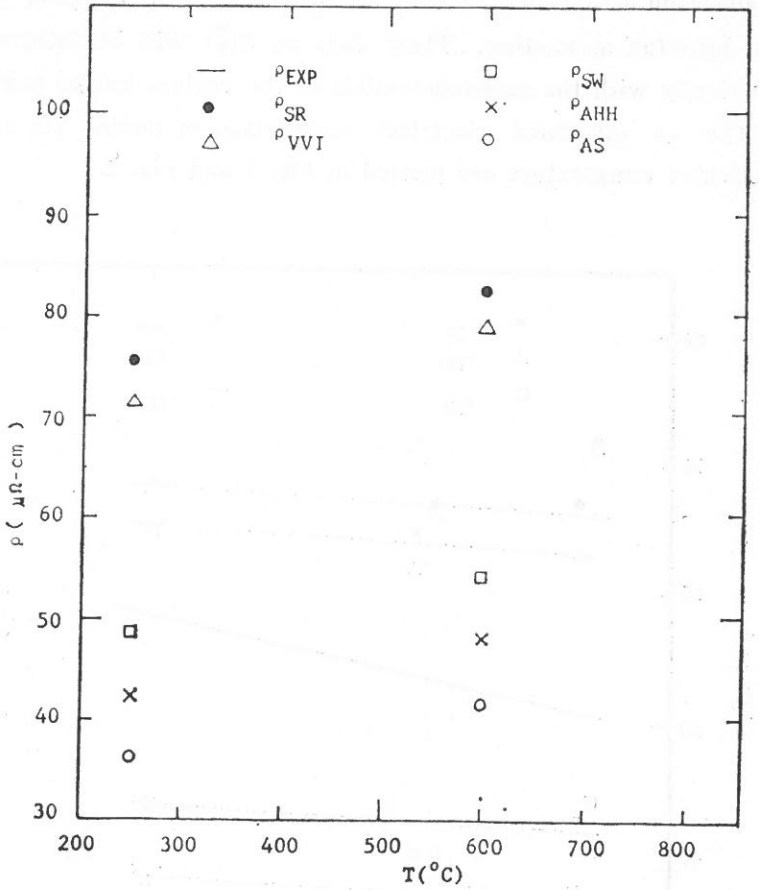

Fig. 2. The temperature dependence of calculated resistivity of liquid Tin for various pseudopotentials with the same scattering structure factor from D. M. North, *et al*, 1968.[2] (ρ_{SR}: Srivastava model; ρ_{VVI}: Simple general model; ρ_{SW}: Shaw model; ρ_{AHH}: Animalu-Heine model; ρ_{AS}: Ashcroft model)

III. THE EXPERIMENTAL MEASUREMENTS OF THE ELECTRICAL RESISTIVITY OF LIQUID TIN

To check the Ziman's theory and look into the temperature dependence of the electrical resistivity of Liquid Tin, we must measure it experimentally.[7]

Our instrumentation set-up is shown in Fig. 3. Resistivity is measured by the DC four-probe technique. Two K-type thermocouples are cemented to the sample holder and are calibrated to given readings within a 0.4°C accuracy. Current is supplied by a stabilized D.C. power supply and monitored by an HP 3478A 5½ digits multimeter. Both the temperature and the voltage are monitored by the HP 3478A DMM. Data are recorded and processed by a microcomputer through GP-IBS. We obtained our pure Tin from Shimakyu Company, Japan. Tin drops are put into a glass tube and are heated under vacuum for more than four days at a temperature

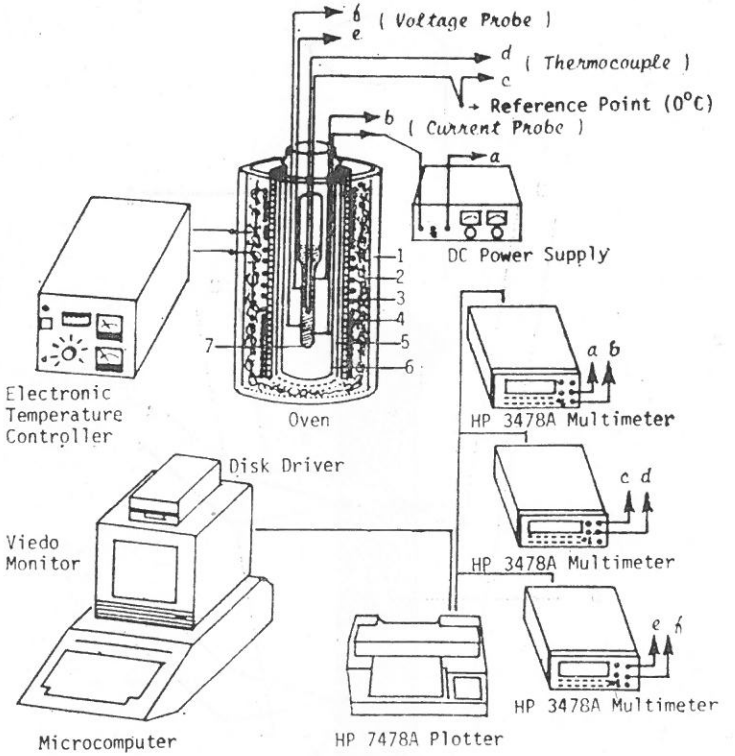

Fig. 3. Instrument Set Up. (1. Aluminum Shell; 2. Ceramic Fiber; 3. Heater; 4. High Temperature Cement; 5. Pyrex Tube; 6. Aluminum Tube, for uniformity of temperature; 7. Sample Holder)

150°C above its melting point. The cleaned sample was checked by S.E.M., X-ray fluorescence and neutron activation. The purity is believed to be better than 99.9%. Then the cleaned sample was poured into a pyrex sample holder as shown in Fig. 4. The system was heated up to 415°C for more than twelve hours for a good wetting among the sample and the electrodes. Then was cooled down stepwise to below its melting point (210°C) at a pace about 20°C per step. At each temperature step the system was allowed to reach its thermal equilibrium and the temperature fluctuation was measured to be within 0.004°C/min. The resistivity was measured

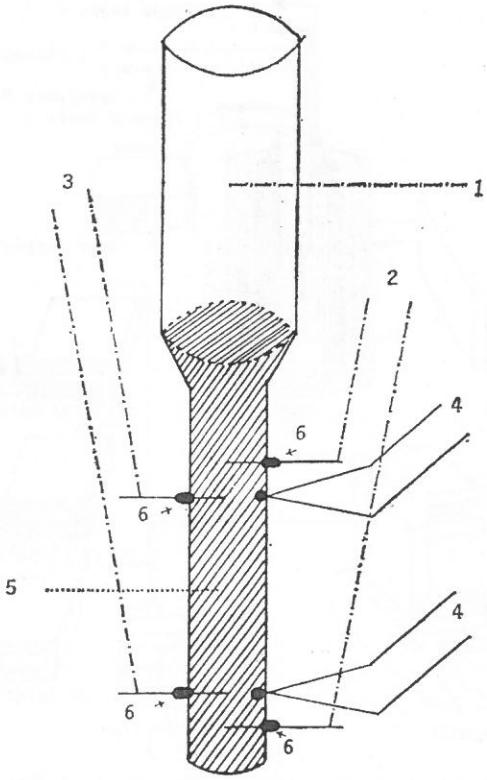

Fig. 4. Sample Holder (1. Pyrex tube; 2. Current Probe; 3. Voltage Probe; 4. Al-Cr Thermocouple; 5. Pure Tin; 6. Pyrex-Tungsten seal)

with both increasing and decreasing temperature and was repeated several times to check the consistency of the system.

IV. RESULTS AND DISCUSSIONS

We made 23 measurements of the electrical resistivity covering a temperature range from 215°C to 410°C, we also made 5 measurements at the melting point. Each measurement of the voltage and current was estimated to be within an error of 0.07% and 0.5% respectively. Resistivity vs. temperature of Tin is shown in Fig. 5.

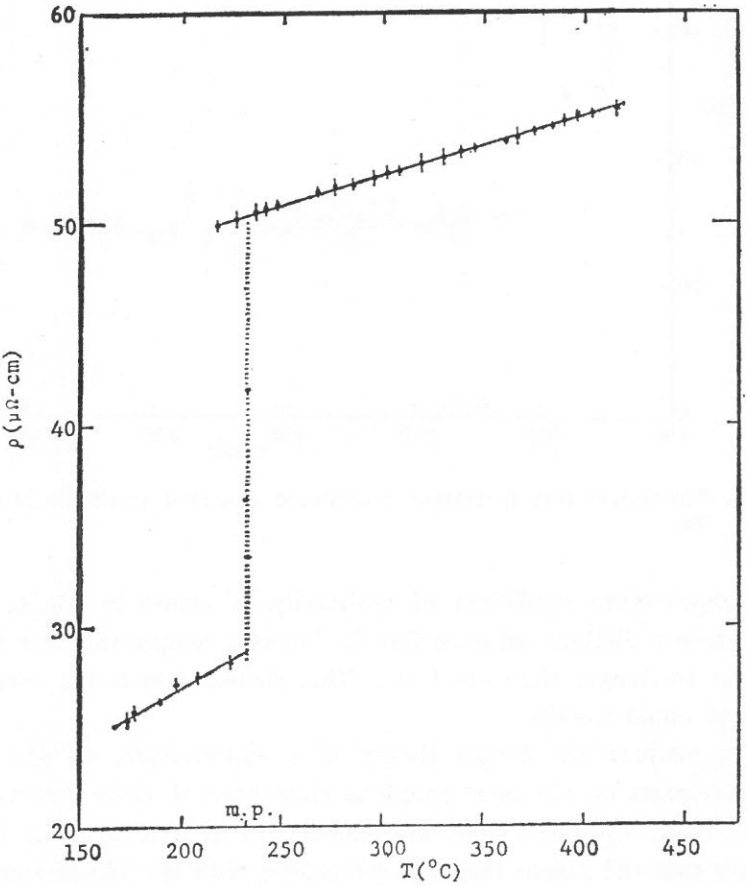

Fig. 5. The temperature dependence of measured electrical resistivity of pure Tin.

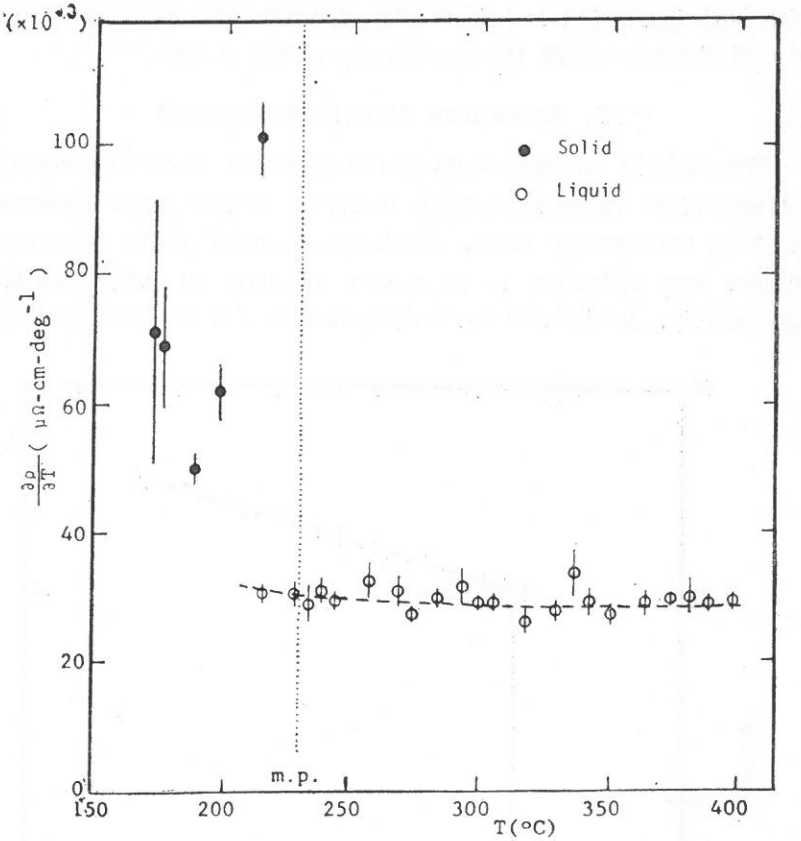

Fig. 6. The temperature derivative of measured electrical resistivity of pure Tin.

The temperature coefficient of resistivity is shown in Fig. 6. We have seen a distinct super-cooling in Tin at a cooling rate less than 16°C/hr for longer than one hour. This phenomenon is not peculiar to most liquid metals.

To compare the Ziman theory with experiments, we plot our measurements on the same graph as that inferred from references (2) and (3), and the results are shown in Fig. 1. From Fig. 1 we can see that the Ziman theory is compatible with our measurements, and in particular, the inferred resistivity ρ_{sw} calculated with Shaw's pseudopotential model agrees with ours fairly.

We notice clearly in Fig. 6 that $\partial\rho/\partial T$ is decreasing as temperature increases. This could be explained by the disappearing of the first peak shoulder of the structure factor as the temperature is increased. Also the lowering values of $S(\vec{q})$ peaks (Fig. 7) causes the integration in Ziman formula to be larger associated with the specific pseudopotential of Tin and could counterbalance the decreasing of $\partial\rho/\partial T$. Since the result is a decreasing $\partial\rho/\partial T$, we could say that the tiny structures in the liquid is vanishing as temperature goes up[5] and this is a very distinct phenomena in liquid Tin.

In Fig. 1 we notice the difference in the slope of calculated and experimental results. This difference may be due to the ignorance of the temperature effect on atomic volumes in our calculations.

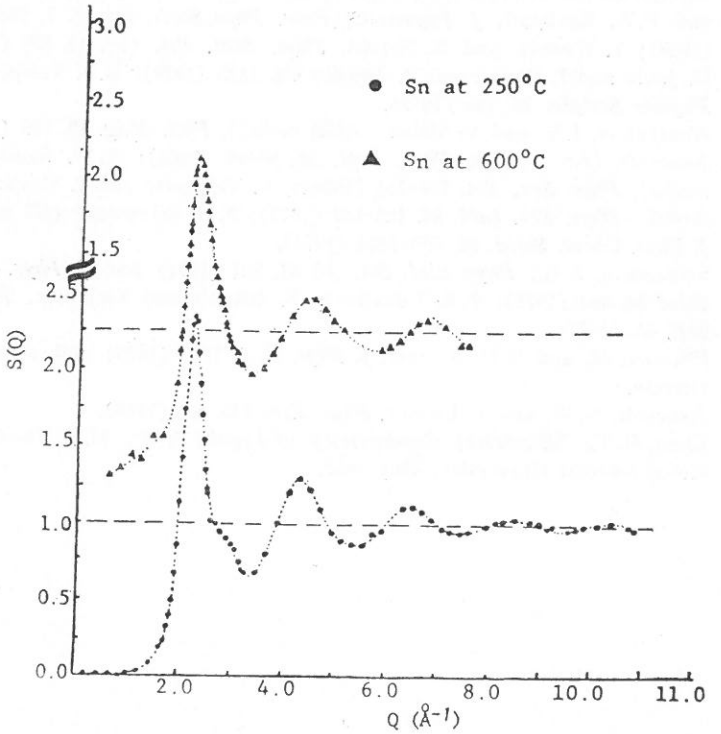

Fig. 7. Structure factors S(Q) for liquid Tin at 250°C and 600°C (D. M. North, *et al*[2], 1968).

We have chosen both the listed atomic volume and the Fermi wave number at melting temperature. Further cautious calculations taking into account the temperature effects are underways.

ACKNOWLEDGEMENT

We thank Dr. S.K. Lai for enthusiastic discussions and for many suggestions from Dr. W.B. Yeung. Also we thank the NSC for its financial support of this project.

REFERENCES

(1) Ziman, J.M., *Phil. Mag.* **6**, 1013 (1961) and also see the book by T.E. Faber, *Introduction to the Theory of Liquid Metals*, Cambridge University Press, 1972.

(2) There are many works done on X-ray diffraction and neutron scattering determinations of $S(\vec{q})$, we quote, in particular, D.M. North, J.E. Enderby and P.A. Egelstaff, *J. Physics C* (*Proc. Phys. Soc.*), Ser. 2, **1**, 784, 1075 (1968); Y. Waseda and K. Suzuki, *Phys. Stat. Sol.* (b), **49**, 339 (1972); D. Jovic and I. Padureanu, *J. Physics* **C9**, 1135 (1976); K.S. Vahvasellka, *Physica Scripta*, **18**, 266 (1978).

(3) Abarenkov, I.V. and V. Heine (AHH model), *Phil. Mag.* **12**, 529 (1965); Ashcroft (AS model), *Phys. Lett.* **23**, 48-49 (1966); R.W. Shaw (SW model), *Phys. Rev.* **174**, 769-781 (1968); V. Veljkovic and I. Slavic (VVI model), *Phys. Rev. Lett.* **29**, 105-107 (1972); S.K. Srivastava (SR model), *J. Phys. Chem. Solid*, **36**, 993-1004 (1975).

(4) Srivastava, S.K., *Phys. Stat. Sol.* (b) **61**, 731 (1974) and *J. Phys. Chem. Solid* **36**, 993 (1975); F.R. Vukajlovic, S. Zekovic and Veljkovic, *Physica* **92B**, 66, (1977).

(5) Plkorny, M. and H.U. Astrom, *J. Phys. F*, **5**, 1327 (1975) and references therein.

(6) Ashcroft, N.W. and J. Lekner, *Phys. Rev.* **145**, 83, (1966).

(7) Chou, H.T., "*Electrical Conductivity of Liquid Tin*", M.S. Thesis, National Central University, May 1983.

A STUDY OF THE EQUATORIAL EVENING MINIMUM IN FARADAY ROTATION RECORDS AND A PRELIMINARY COMPARISON OF RECORDS FROM WIDELY SPACED STATIONS*

JOHN R. KOSTER SVD

ABSTRACT

The Equatorial Evening Minimum (EEM) appears in Faraday Rotation measurements made near the magnetic dip equator, and is closely associated with a plasma instability which gives rise to severe scintillations in radio signals. An attempt is made to study this phenomenon on a worldwide basis. This is done in the hope that EEM measurements, which are easily made (and are available also in Taiwan) can be used as an accurate predictor of scintillations at all stations within about 20° north or south of the dip equator. This attempt, if successful, will be of great practical use in predicting communication conditions and in designing communication and other (e. g. radar) systems which depend on the transmission of signals through the ionosphere in a broad belt centered on the dip equator. This paper reports encouraging progress in this endeavor and suggests that the program may lead to very practical results as well as to a better understanding of the physical factors contributing to the severe scintillations experienced near the equator.

INTRODUCTION

The Nature of the EEM and its Measurement:

One of the largest disturbances in the equatorial ionosphere occurs shortly after ionospheric sunset. It has been found by McClure *et al.*[1] that large plasma "bubbles" are formed in the lower ionosphere. These bubbles are regions in which the electron density may be as much as three orders of magnitude smaller than

* A paper prepared for submission at the International Symposium on Beacon Satellite Studies of the Earth's Environment, New Delhi, India, Feb. 7-11, 1983.

that of the ambient medium. Once formed, the bubbles frequently rise through the ionosphere, giving rise to large amplitude and phase scintillations of radio signals, "plumes" on the radar power maps similar to those discovered by Woodman and LaHoz[2] and deep minima in the TEC as determined from the Faraday rotation of radio signals as described by Koster[3-5]. The phenomenon is relatively regular in time and appears not only in daily TEC plots, but may also be seen quite clearly in the monthly mean values of TEC for most months at an equatorial station. We shall hereafter refer to this phenomenon as the equatorial evening minimum (EEM).

The method of measuring the EEM adopted in this paper is the following: Take the portion of the daily (or monthly mean) TEC plot from the afternoon maximum to the pre-sunrise minimum —normally from 15H local time to 05.30H the following day. A smooth, monotonically decreasing curve is fitted to the data points. A function of the form:

$$Y = C + A \cdot \tanh(\alpha + \beta x + \gamma x^2)$$

has been found satisfactory. Values of C and A are chosen by a method of successive approximation. The three parameters in the argument of tanh are determined by standard least squares methods. The numerical value of the EEM is the "badness" of fit of the smooth curve to the data points. It is defined as 100× the rms difference between the data points and the curve, divided by the rms sum of the data points. Points between 18H local time and 24H local time were used for this calculation. Fig. 1 and 2 show monthly mean plots derived from Waltair data and the corresponding smooth curves fitted as described.

SUMMARY OF PREVIOUS FINDINGS

Previous work by Koster[5] has come to the following conclusions about the EEM:

a) The value of EEM has a large seasonal variation. A plot of monthly mean EEM is very similar in shape to plots of monthly occurrence frequency of deep scintillations, at least for the

African station (Legon) investigated.

b) The value of EEM varies very little with sunspot cycle.

c) There is some dependence on satellite elevation. A satellite observed at a very low elevation angle has a diminished value of EEM.

d) There is a large difference between EEM values from widely

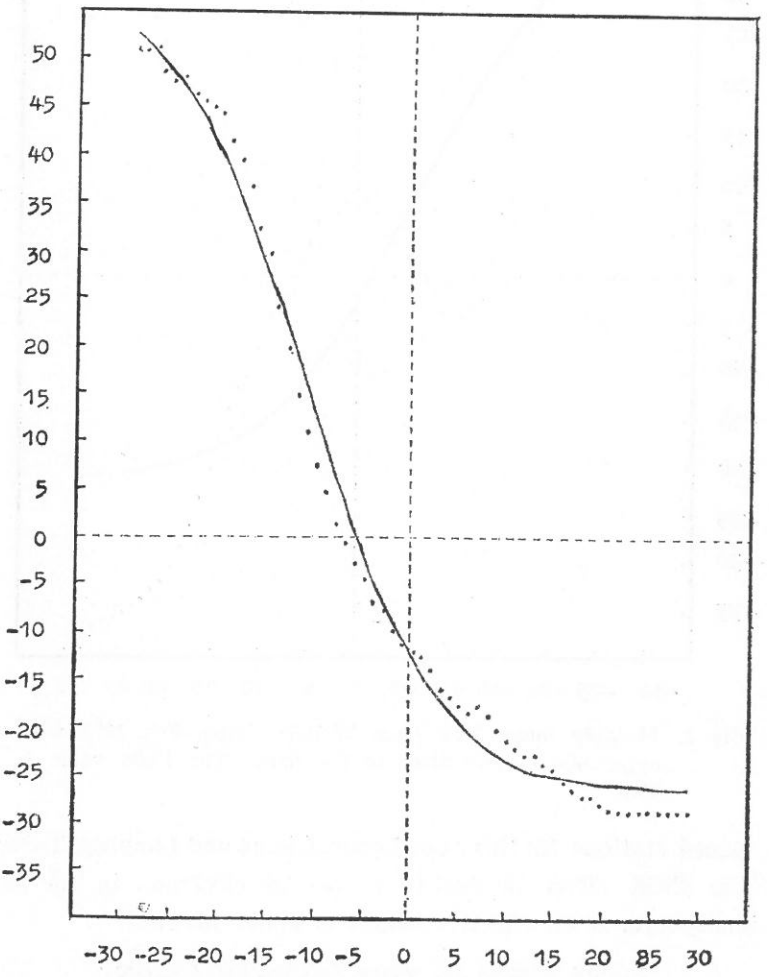

Fig. 1. Monthly mean TEC from Waltair, India, June 1978, with hyperbolic tangent fitted to the data. The EEM value is 8.2.

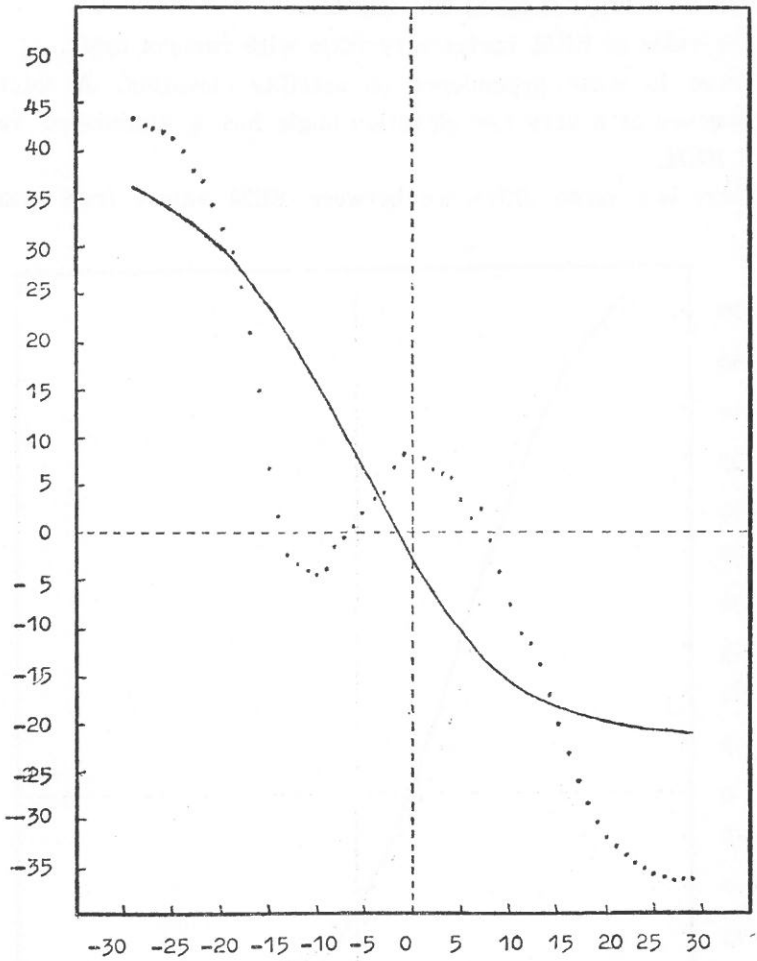

Fig. 2. Monthly mean TEC from Waltair, India, Feb. 1979, with hyperbolic tangent fitted to the data. The EEM value is 33.3.

spaced stations (in this case, Legon, Ghana and Lunping, Taiwan).

e) The EEM effect is due to a loss of electrons in the lower ionosphere, at an effective height of about 100 km.

DATA USED IN THIS INVESTIGATION

The table below summarizes the TEC data used in the present investigation.

Table 1. Summary of Stations and Data Used in the Present Investigation

Station	420 km point		Elev	Satellite	Dates
	Long.	Dip			
Legon	− 10.0°	− 8.0°	12.0°	ATS/3;ATS/5	July '69-Jun. '78
Legon	− 1.3	− 8.7	71.4	Sirio	July '78-Jan. '79
Lunping	122.0	31.1	59.2	ETS-2	Mar. '77-Dec. '79
Manila	121.7	11.8	69.9	ETS-2	May '81-Feb. '82
Asc. Is.	− 14.4	−27.6	80.7	Sirio	May '80-Apr. '81
Waltair	88.3	16.4	33.6	ETS-2	Mar. '78-Feb. '79

RESULTS OF THIS INVESTIGATION

(a) The Dependence of EEM on Sunspot Numbers

An unbroken series of 82 monthly mean values of TEC was used. The data were all taken at Legon, Ghana, using the satellites ATS-3 and ATS-5, between September 1971 and June 1978. The elevations of the satellites were 12 degrees throughout the period. During this time, the monthly mean sunspot number varied between values of 2 and 99. Statistical analysis shows that a small positive dependence of EEM on sunspot numbers does exist. Variations in sunspot number between 0 and 100 lead to variations in EEM of ±12% around the mean. In all the following investigations, EEM values were reduced to a mean sunspot number of 50 using the above dependence. A linear dependence was assumed.

(b) The Dependence of EEM on Satellite elevation

Figure 3 summarizes the results of the investigation of the dependence of EEM on satellite elevation. All data were from Legon, Ghana. The circles represent the mean values of EEM for each month. Seven years of continuous data were used, all from the satellites ATS-3 and ATS-5 at an elevation of 12°. The error bars represent ±1 standard deviation about the mean. All data are corrected to a monthly mean sunspot number of 50. The squares show seven months of EEM values from SIRIO, at an

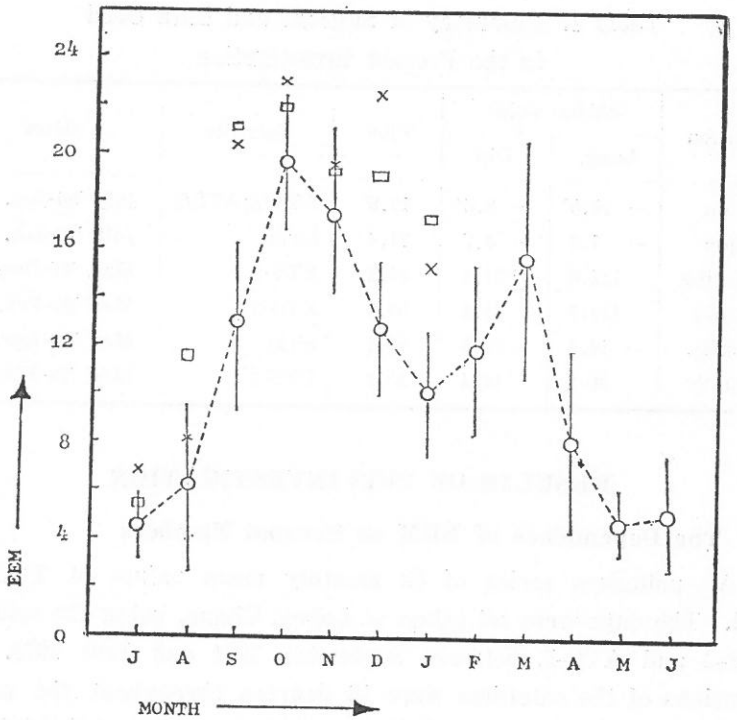

Fig. 3. Dependence of EEM on satellite elevation at Legon. ○=ATS-3/5 at 12° (7 years of data); □=Sirio at 70°; × =ATS-3 at 38°.

elevation of 70°; the x's show values of EEM from ATS-3 at a time when its elevation was 38°. From the figure, we conclude that there is definitely a dependence of EEM on satellite elevation since:

1. All results from the satellite at 70° are higher than those from the satellite at 12°, even after correction for sunspot numbers.
2. In 4 of the 7 months the difference exceeds one standard deviation.
3. All results from the satellite at 38° elevation are also higher than those taken at 12°.
4. In 5 out of the seven cases, the difference exceeds 1 standard deviation.

We note that there is no statistically significant difference

between the results obtained at 38° and those obtained at 70°. It would therefore seem that elevation need only be taken into account in the case of satellites at very low angles of elevation.

(c) The Variation of EEM with Latitude

To determine whether EEM is a function of latitude (or rather, of dip angle) two sets of data from stations at nearly identical longitudes, but widely differing dip angles were compared.

In the first comparison EEM values from Legon (dip −8.7°) were compared with those from Ascension Island (dip −27.6°). A plot of the results appears as Fig. 4 Both stations were observing SIRIO. It is to be noted that the values from Legon are larger by a factor of 2.37±0.26.

Fig. 5 shows corresponding plots of EEM from Lunping, Taiwan (dip 31.1°) and from Manila (dip 11.8°). The Manila data are larger by a factor of 3.02±1.42.

The following features are noted in the diagrams:

1. At both longitudes there is a marked dependence of EEM on latitude (or more accurately, on dip angle).
2. At dip angles of the order of 30°, the EEM has almost entirely disappeared. It should be noted that values of EEM between 0 and about 6 or 7 can be attributed to noise in the data, and correspond to no discernible EEM in the plots.
3. At relatively small dip angles the value of EEM is large, typically between 20 and 30 in equinoctial months.
4. The amplitudes in the two sectors are almost equal, with no statistically significant difference discernible in the (admittedly inadequate) data.
5. The seasonal variation for the African sector (Legon) appears most clearly in Fig. 3, only partially in Fig. 4. The Asian sector seasonal variation appears in Fig. 5. Data used are insufficient to give a very precise picture of the seasonal dependence in the Asian sector, but the indications are that there are significant differences in the two sectors. Data should soon be available to clarify this point.

(d) The Correlation of Daily EEM with Scintillation

Thus far we have considered only those values of EEM which were determined from monthly mean TEC data. We now turn our attention to values of EEM resulting from the analysis of daily TEC data. This work is still incomplete, but some results can be reported here.

Daily scintillation data were obtained at Legon from the Satellite MARISAT 1 (elevation 70°) for 15 months from March 1977 to June 1978. The frequency used was 257 MHz—high enough to avoid most of the saturation effects experienced at low latitude stations when using 136 MHz. Since the MARISAT signal was circularly polarized, no Faraday measurements were possible. But another satellite (ATS-5) was being observed at Legon at the same time, and TEC determinations were made using its 136 MHz radiated signal.

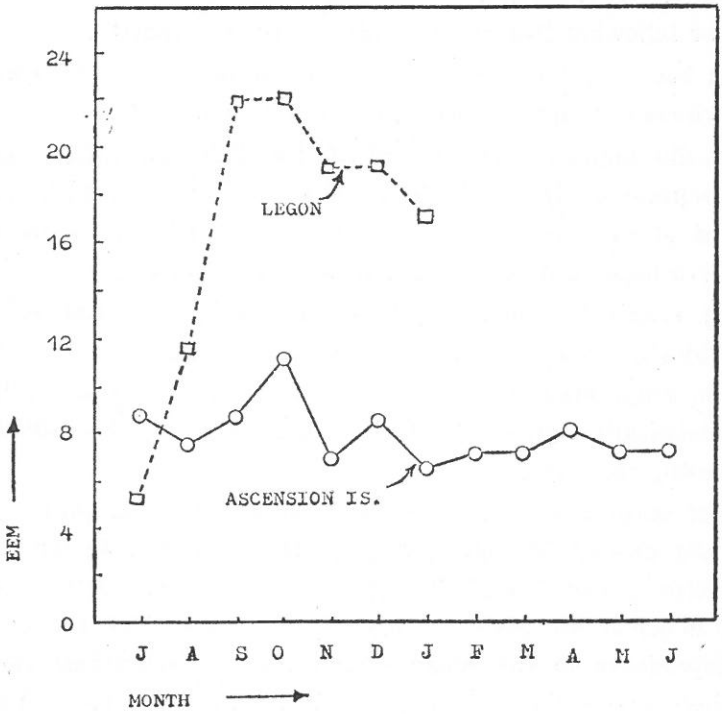

Fig. 4. Latitude dependence of EEM—Legon and Ascension Is.

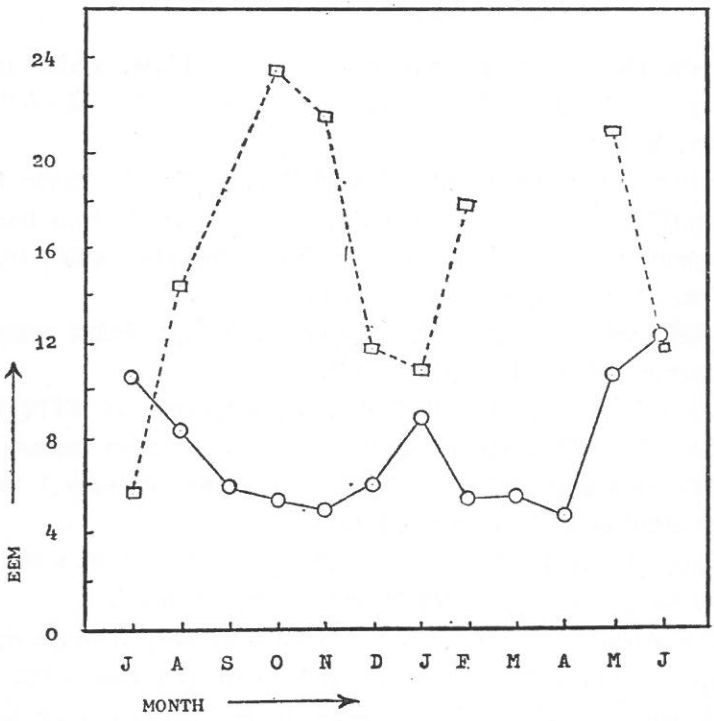

Fig. 5. Latitude dependence of EEM—Manila (□), Lunping (○).

Although the 420 km subionospheric points for the two satellites are separated by nearly 1,000 km, one should recall that EEM is produced by a loss of electrons at the 100 km level. Hence the EEM observed at an angle of elevation of 12° is due to a loss of electrons in the E region only a few degrees of longitude to the west of Legon. Hence, MARISAT scintillation was correlated on a day to day basis with EEM as determined from ATS-3. The parameter actually used to specify scintillation in this case was the number of 15-minute intervals between 20H and 24H local time having scintillation indices greater than 6 db.

The correlation coefficient for 471 days is 0.41—significant even on the 0.1% level. Of the 15 monthly intervals taken separately, 8 showed positive correlation significant on the 10% level.

SUMMARY AND CONCLUSIONS

From the above, we conclude that the EEM, which can be relatively easily derived from TEC measurements, has the following characteristics:

1. It has a very large seasonal variation, similar in shape to the scintillation versus season plots. There seems to be a longitude dependence, but this has not yet been adequately explored.
2. There is a small sunspot cycle dependence.
3. EEM varies strongly with dip angle. It has almost completely disappeared at dip angles of 30°.
4. There is a moderate diminution in amplitude of EEM in the case of satellites observed at very small elevation angles.
5. Maximum amplitudes of EEM (around the equinoxes) are not strongly dependent on longitude.
6. There is very strong correlation with the deep scintillation normally associated with "bubbles" and "plumes".

The day-to-day connection of EEM with deep fading must still be explored in much more detail. It is suggested that EEM determined from data obtained at or near the dip equator may well be a useful predictor of severe scintillation for all stations within ±15° of the dip equator at that longitude.

Since TEC measurements are widespread, relatively objective, and independent of instrument characteristics they are much easier to use than scintillation measurements. In the EEM we have a very useful parameter which can be extracted from TEC measurements. If used in the analysis of the large amount of TEC data now available, it should prove very valuable in clearing up some of the obscurities still shrouding the global picture of scintillation and the phenomena associated with it.

ACKNOWLEDGEMENTS

Sincere thanks are expressed to Dr. Yinn-Nien Huang for kindly providing three year's of data from Lunping, Taiwan; to Dr. P. V. S. Rama Rao, for providing a year's data from Waltair, India, and to

Dr. J. Klobuchar for providing one year's data from Ascension Island and Manila. Thanks are also due to the University of Ghana for kindly allowing the use of Legon data.

REFERENCES

(1) McClure, J.P., Hanson, W.B., and Hoffman, J.H. *J. Geophys. Res.* 82 (1977), 2650.
(2) Woodman, R.F., and LaHoz, C. *J. Geophys. Res.* 81 (1976), 5447.
(3) Koster, J.R. *Fu Jen Studies* 7 (1973), 1.
(4) Koster, J.R. *Proceedings of the Symposium of the Cospar satellite beacon group.* Beacon satellite measurements of plasmaspheric and ionospheric properties. Firenze, Italy, 1978.
(5) Koster, J.R. *Fu Jen Studies* 15 (1981), 35.

It is the age of Socrates again: *Our moral life* is threatened, and our intellectual life is quickened and enlarged by the desintegration of ancient customs and beliefs. Everything is new and experimental in our ideas and our actions; nothing is established or certain any more.

Our culture is superficial to-day, and our knowledge dangerous, because we are rich in mechanisms and poor in purposes. The balance of mind which once came of a warm religious faith is gone; Science has taken from us the supernatural basis of our morality, and all the world seems consumed in a disorderly individualism that reflects the chaotic fragmentation of our character.

We move about the earth with unprecedented speed, but we do not know, and have no thought, where we are going, or whether we shall find any happiness there for our harassed souls.

WILL DURANT

MICROCOMPUTER CAI FOR CHINESE LANGUAGE WITH CHARACTER GENERATOR

YEONG-WEN HWANG

ABSTRACT

This paper describes a CAI system for Chinese language. The system utilizes a true character generator with unlimited character numbers. It is built on a home computer with very compact memory size and low cost. Cassette tapes are used for inputing CAI lessons.

System software and hardware allow various types of lessons, interactive messages, multiple hints, random selection, scoring, 16 colors, sound effects, 50 special symbols per each tape, diagrams with straight line and circular segment generators plus dot-by-dot plotting ability. The CRT displays 8 lines of 16 Chinese characters/line with easy roll-up, erase, flash, redisplay and other screen managements.

The internal software formats of the assembly-written system are explained in detail. The system is successfully implemented. Sample pictures taken in black & white are shown.

1. GENERAL DESCRIPTION

In English language, CAI systems are well developed. It is quite needed that such systems be developed for Chinese language. Such work is only in its beginning stage. In view of the situation here, it is best to implement the system on a microprocessor-based home computer.

This paper describes a successfully developed CAI system on a Z80 microcomputer. Lessons are read into the computer through cassette tapes. In this way we can have a CAI in home situation, with independent study, and at low cost.

The system is completely interactive. Users choose the tape containing the subject they want to learn. The main program is recorded in the head part of each tape followed by several lessons. Loading of a tape will bring the system into the computer. The system then asks about which lesson it is going to study this time,

and will continue to look for the identification of that lesson until it is found. Users may skip lessons by fast-forward tape operation to the desired position to save time.

Most Chinese systems require too much memory to be practical in this application. Limitation on number of characters also present a serious drawback. Hence this computer uses a GCS Chinese Character Generator which is very compact (<12k Bytes) and has virtually no character number limits.[1]

A software service routine package is written for an easy use of this character generator. The CAI main program calls these routines to manipulate characters on the screen. This relation is shown in Fig. 1. The character generator also generates 128 ASCII characters in larger size (7×11) to go with Chinese characters (14×16).

An ordinary TV may be used as the display element, although a monitor can also be connected. The format of screen display is as shown in Fig. 2 if Chinese characters are to be shown all over the screen. Though a full screen is limited to 16 by 8 Chinese characters, users can easily roll-up the screen display or choose to redisplay a problem from the beginning at any time. This manouvre ability compensates the limited screen size. Pressing the roll-up key rolls up the text portion of the problem continuously until the user

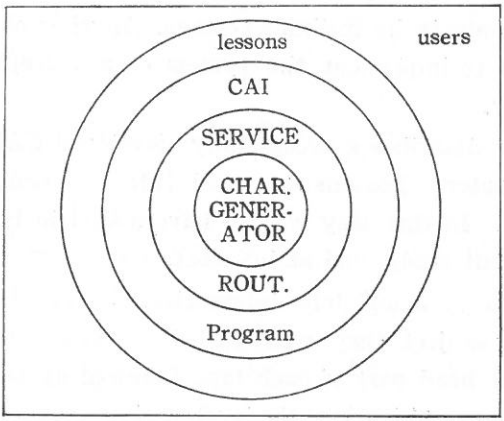

Fig. 1. Software structure.

in IC 9918. All programs are written in assembly lauguage.

The internal format of a problem is as follows:
F3, F3, F3, problem type, score, diagram type, line type, ... line data..., line type, ...line data..., ..., FF, character identifier, character color, ... character codes..., F3, F3, answer identifier, ...answer..., F3, hint type, ...hint data..., F3, hint type, hint data... ,

where *problem type*:

=0: single choice problem
=1: multiple choice problem
=2: fill-in space type

score:

=1~9: the score of this problem;

diagram type:

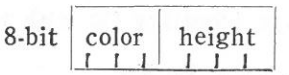

height =0: no diagram
=1~6: diagram height in lines;

line type and data:

Type	Meaning	With data
C 0	circle	Yc, Xc, R
C 1	$\frac{1}{4}$ circle, 1st quadrant	Yc, Xc, R
C 2	$\frac{1}{4}$ circle, 2nd quadrant	Yc, Xc, R
C 3	$\frac{1}{4}$ circle, 3rd quadrant	Yc, Xc, R
C 4	$\frac{1}{4}$ circle, 4th quadrant	Yc, Xc, R
C 5	$\frac{1}{2}$ circle, upper half	Yc, Xc, R
C 6	$\frac{1}{2}$ circle, left half	Yc, Xc, R
C 7	$\frac{1}{2}$ circle, lower half	Yc, Xc, R
C 8	$\frac{1}{2}$ circle, right half	Yc, Xc, R
C A	arc in 1st quadrant	Yc, Xc, R, Y1, Y2
C B	arc in 2th quadrant	Yc, Xc, R, Y1, Y2
C C	arc in 3rd quadrant	Yc, Xc, R, Y1, Y2
C D	arc in 4th quadrant	Yc, Xc, R, Y1, Y2

Type	Meaning of data
C 0	Center coordinates, radius
C 1	Center coordinates, radius
C 2	Center coordinates, radius
C 3	Center coordinates, radius
C 4	Center coordinates, radius
C 5	Center coordinates, radius
C 6	Center coordinates, radius
C 7	Center coordinates, radius
C 8	Center coordinates, radius
C A	Center, radius, Y coordinates
C B	Center, radius, Y coordinates
C C	Center, radius, Y coordinates
C D	Center, radius, Y coordinates

where Y1, Y2 are y coordinates of the arc, starting and ending as in Fig. 3.

Straight line has the type identifier D0 with the data format:

D0, Y1, X1, Y2, X2, ..., Yn Xn

where Yi, Xi are the coordinates of a break-point on a break-line. Instead of stating the beginning point and ending point of each line which takes 4 bytes, only the beginning point of the first line is stated if other beginning points coincide with the ending points of their preceeding ones, otherwise more D0 identifiers are needed.

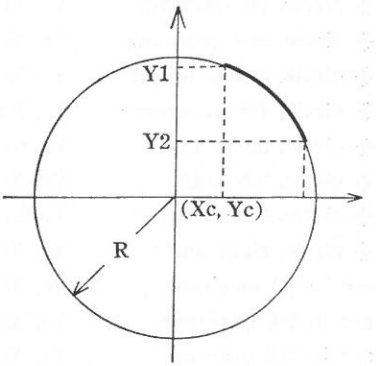

Fig. 3. Arc expression.

This arrangement will in general save memory spaces.

The screen has 256×192 dots. Y coordinates are always listed as the first of the coordinate pairs. Since Y is between 0 and 191 (or BF), it would not mix up with identifiers which are above C0.

5. ADDED FUNCTIONS

The system accepts a direct 8×8 pattern plot. It also allows up to 50 arbitraryly defined symbols for each tape, either 8×8 or 8×16 matrix, such as shown in Fig. 4. Furthermore, Chinese characters are allowed to appear in the diagram provided they are at their regular positions as shown in Fig. 2.

Problem writers may choose to flash a particular line in the diagram on and off several time to cause the user's special attention, or may erase the diagram and re-draw it differently.

The following codes are for such functions and their accompanying data formats:

Code	With data
E 0	Y1, X1, 8 bytes
E 1	Y1, X1, Symbol type, Symbol code(s)
E 2	Char. start position, character string, F3

Code	Meaning of data
E 0	Plot 8 bytes at Y1, X1 position.
E 1	Plot defined symbol at Y1, X1 position.
E 2	Show character string in the diagram.
E E	Erase the diagram.
E F	Flash the line just displayed.

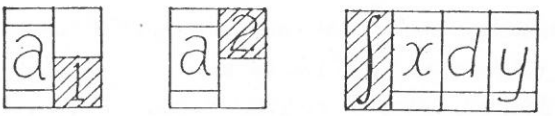

Fig. 4. Special symbols (in shadow).

where *symbol type* =0: 8×16 full height
=1: 8×8 at upper position
=2: 8×8 at lower position
=3: 8×16 made from two 8×8 symbols, two codes to follow.

symbol code is one of the 50 codes defined for symbols.

The character start position is defined by Fig. 2 and has the format as

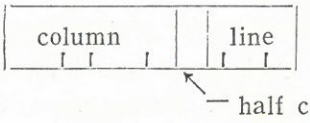

6. HINTS

In case the user's answer is wrong, the user may be given hints in several ways. A sentence, a diagram or both may be given, or no hint is given, depending on the problem design. The hint may be general, given twice, or special to specific answer. The computer shows the right answer the third time. The format of hint is F3, hint type, ...hint data..., F3, hint type, ...hint data..., following the answer, where

hint type =1~6: Special hint for the specific answer number 1 to 6.
=7 : First general hint.
=8 : Second general hint.
=9 : Explanation.

hint data is in the form:
character identifier, color, ...character codes...

with the same format as in the problem text. The character string of hint is shown on the last line which is used as the answer and hint line.

The explanation notifies the computer that the answering message is with the diagram and has the form

F3, 9, diagram type, ...diagram data..., FF, ...character data .....

7. OTHER ASPECTS

The system picks up and shows the problem at completely random order. Each time users start the same lesson they see different problem combinations and order. In the same run, a problem already studied will never be picked up again.

Each problem is given a score. Full score is given when the user is right the first time. The score decreases as the number of times increases. When the total score (counting full score) comes to 100 (or a little more), the program ends a run. The user's score versus full score is always shown on the screen. So is the score of the present problem. Users may also check a displayable score list-table which shows scores of several runs practised.

Answering time can be taken into account. If the second scheme is chosen by the user, time is counted. No score is given if the time limit is exceeded.

Music accompanies the program. Turn off the volume switch of the TV to disregard the music.

8. HARDWARE

The system uses a Z80A as cpu with 16KB ROM for system program and 24KB RAM for tape loading. It employs 8910 as tape, keyboard and sound interface, 9918 as display control interface with 16KB more display RAM. The Alpha-numerical Keyboard can be used to imput Chinese (components are assigned to keys as well

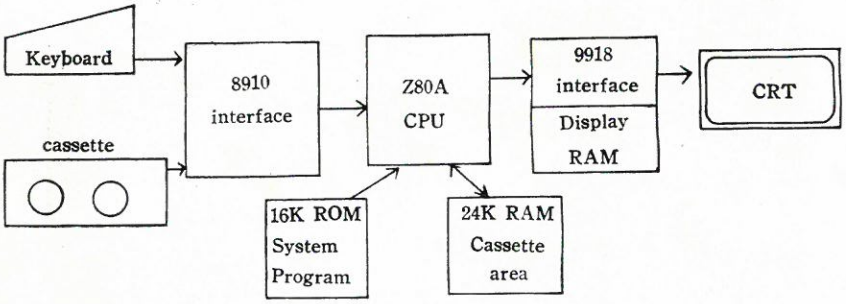

Fig. 5. System hardware.

as alphabets) and there is a printer interface to print characters, but they are only used for developing the system. To the CAI user, neither is needed.

Fig. 5 is the block diagram of the system.

9. RESULTS

The system was implemented and tested. It fullfills the specifi-

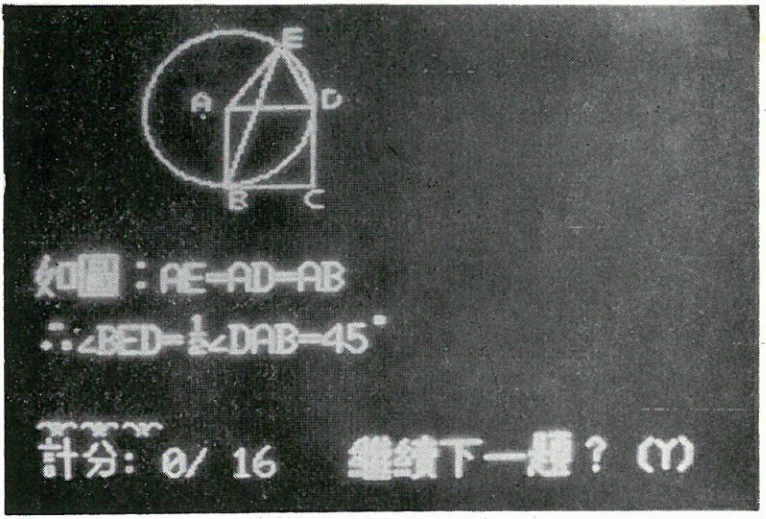

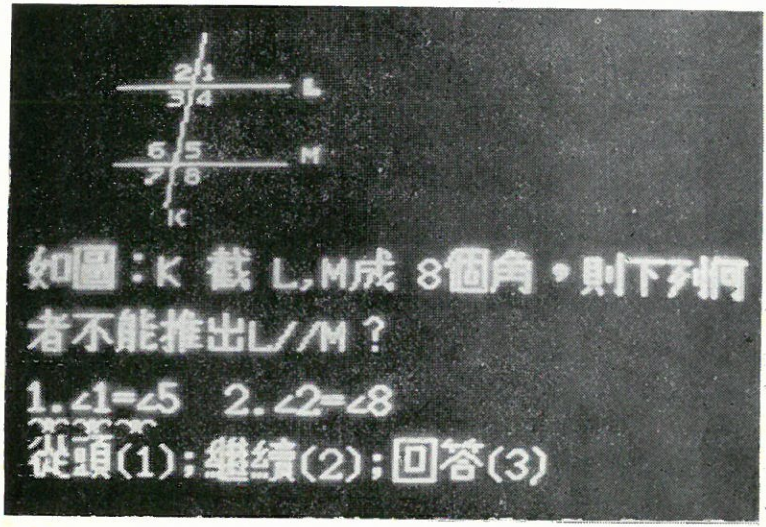

cations described. Several photos show the typical screen outputs in black & white.

It is found that an auxiliary program is to be written to help problem writers in keying-in their data. Also, formated paper forms may be printed for CAI lesson writers.

REFERENCES

(1) *A New Component System with Geometrical Grammar and Improved Character Appearance*, Y. W. Hwang, P362-368, Proc. of International Computer Symposium, Taipei, 1975.

(2) *A Baxic Graphic System*, Frank Na, P. 989-996, Proc. of International Computer Symposium, Taipei, 1977.

Man in this moment of his history has emerged in greater supremacy over the *forces of nature* than has ever been dreamed of before. There lies before him, if he wishes, a golden age of peace and progress. He has only to conquer his last and worst enemy—himself.

The only guide to a man is his *conscience;* the only shield to his memory is the rectitude and sincerity of his actions. It is very imprudent to walk through life without this shield, because we are so often mocked by the failure of our hopes, but with this shield, however the Fates may play, we march always in the ranks of honor.

We shall go forward together. The road upward is long. There are upon our journey dark and dangerous valleys through which we have to make and fight our way. But it is sure and certain that if we *persevere*, and we shall persevere, we shall come through these dark and dangerous valleys into a sunlight broader and more genial and more lasting than mankind has ever known.

WINSTON CHURCHILL

CONTRIBUTORS TO THIS NUMBER

Wen-Jen Lin 林文仁, graduate student in physics at Fu Jen University.

Kung-Tung Wu 吳坤東, associate professor of physics at Fu Jen University.

Jen-I Chen 陳振益, professor of physics at Fu Jen University.

Hsueh-Tau Chou 周學韜, graduate student in physics at the Central University, Chungli, Taiwan.

Tai-Sone Yih 易台生, associate professor of physics at the Central University, Chungli, Taiwan.

Sheau-Huey Chia 賈小慧, lecturer in physics at Fu Jen University.

John R. Koster, SVD, 高士達, professor of physics and director of the Computer Center of the College of Science and Engineering at Fu Jen University.

Yeong-Wen Hwang 黃永文, professor of electronic engineering and chairman of the Department of Electronic Engineering at Fu Jen University.

PRINTED BY

Ching Hua Press Co., LTD., Taipei